NATIONAL AND KAPODISTRIAN UNIVERSITY OF ATHENS

SCHOOL OF SCIENCE
DEPARTMENT OF INFORMATICS AND TELECOMMUNICATION

MSc THESIS

AI/ML assisted Li-Fi communication systems for the future 6G communication systems

Khojiakbar B. Botirov Sanjar

Supervisors: **Dimitris Syvridis,** professor
Panagiotis Stamapoulos, professor

ATHENS

September 2021

MSc THESIS

AI/ML assisted Li-Fi communication systems for the future 6G communication systems

Khojiakbar B. Botirov Sanjar

S.N.: 1200005

SUPERVISORS: **Dimitris Syvridis,** professor
Panagiotis Stamapoulos, professor

ABSTRACT

Information and communication technologies are developing rapidly, and tremendous growth along with advancements was observed over the last few decades. Requirements for bandwidth and capacity of current networks are overgrowing due to the increase in the use of high-speed Internet, video conferencing, streaming, Internet of things, etc. An ever-growing demand for increasing data volumes and multimedia services has led to an overload in the traditional radio frequency (RF) spectrum is used, and there is a need for transition from RF carrier to optical media. In this work, novel Deep Neural Network (DNN) was proposed to mitigate nonlinearities caused by Perovskite material-based components of Li-Fi communication system, and measurement of Perovskite Photodiodes (PePD) the Optical Communications Laboratory in the National and Kapodistrian University of Athens. Due to the analysis of the PePDs bandwidth measurement, the highest cut-off frequency was measured 36,25kHz at 635nm wavelength. The proposed DNN showed promising results in comparison with Support Vector Machines (SVM) model, both models were trained on the dataset generated by OFDM based - Li-Fi systems. This technique successfully mitigates the nonlinearity of the PePD and the interference generated by the multipath channel. The simulation results reveal that the proposed scheme outperforms conventional techniques in terms of BER performance demonstrating the potential and validity of DL in the Li-Fi system.

SUBJECT AREA: Wireless Optical Networks, Deep Learning

KEYWORDS: Li-Fi, PePD, PeLED, DNN

I dedicate my dissertation work to my family. To my parents, Sanjar, and Nigora. Their words of encouragement and support pushed me to do better and be the person I am today.

ACKNOWLEDGMENTS

I would like to thank my supervisor Prof. Dimitris Syvridis and Panagiotis Stamapoulos for great help, exceptional motivation, and valuable advice given during our hard work.

I would like to thank my co-supervisors Dr. Nikolaos Raptis and Stylianos Kazazis for creative ideas, incredible driving force, professional advice, great help.

I would like to thank my colleague Afnan Amayreh for a valuable contribution to the work, many hours of work together and a great experiment.

This Master Thesis has been accomplished in the framework of the European Funded Project: SMART Telecom and Sensing Networks (SMARTNET) - Erasmus+ Programme Key Action 1: Erasmus Mundus Joint Master Degrees – Ref. Number 2017 – 2734/001 –001, Project number - 586686-EPP-1-2017-1-UK-EPPKA1-JMD-MOB, coordinated by Aston University, and with the participation of Télécom SudParis, member of IP Paris and National and Kapodistrian University of Athens.

CONTENTS

LIST OF FIGURES

LIST OF TABLES

1. INTRODUCTION

Due to the increasing demand for wireless data communication, the available radio spectrum below 10 GHz (cmwave communication) has become insufficient. The wireless communication industry has addressed to this obstacle by investigating radio frequencies greater than 10 GHz (mm-wave communication). The higher the frequency, the greater the path loss, according to the Friis free space equation (L f2). Additionally, at higher frequencies, obstructions and shadowing in terrestrial transmission are more difficult to overcome. As a result, systems must be built to maximize the likelihood of line-of-sight (LoS), which is generally accomplished by the use of beamforming methods and the use of extremely tiny cells (approximately 50 m in radius). From a system capacity standpoint, the requirement for tiny cells is irrelevant. This is because shrinking cell sizes has undoubtedly been the primary factor in improving system performance in modern cellular communications. Contrary to popular belief, this means that using higher frequencies for terrestrial communication has become a viable alternative. However, one drawback is that the task of sustaining ever-smaller cells becomes considerable. Providing advanced backhaul infrastructure is one such example. Light-fidelity (Li-Fi) [is a continuation of the electromagnetic spectrum's movement toward higher frequencies.
Li-Fi is a kind of nm-wave communication. Li-Fi employs light emitting diodes (LEDs) for high-speed wireless communication, and rates of over 3 Gb/s have been shown utilizing optimized direct current optical orthogonal frequency division multiplexing (DCO-OFDM) modulation on a single micro-light emitting diode (LED) [3]. Given the increasing use of LED lighting in homes, workplaces, and streetlights due to their energy efficiency, Li-Fi cellular deployment has the added benefit of being able to leverage existing lighting infrastructures. Additionally, compared to mm-wave communication, cell sizes can be decreased further, resulting in the notion of Li-Fi attocells. Li-Fi attocells act as an extra network layer within existing heterogeneous wireless networks, causing no interference with or adding to their radio frequency (RF) equivalents, such as femtocell networks. A Li-Fi attocell network makes advantage of the lighting system to enable fully networked wireless connection (multiuser access and handover).

1.1 From VLC to Li-Fi

VLC employments LEDs to transmit information wirelessly by utilizing intensity modulation (IM). At the photodiode, the signal is recognized by a photodiode (PD) and by utilizing the principle of direct detection (DD). VLC has been conceived as a point-to-point information communication technique – basically as a cable substitution. This has driven to early VLC standardization exercises as portion of IEEE 802.15.7 [6]. This standard, in any case, is as of now being revised to incorporate Li-Fi. Li-Fi in differentiate portrays a total wireless networking framework. This incorporates bi-directional multiuser communication, i.e. point-to-multipoint and multipoint-to-point communication. Li-Fi also includes various access points to form a remote system of extremely small optical cells with sequential handoff. This implies that Li-Fi empowers full client portability, and so shapes a modern layer inside the existing heterogeneous wireless systems. The fact that LEDs are characteristic beamformers enables neighborhood control of Li-Fi signals, and because of the blockage of the signals by

opaque walls, co-channel interference (CCI) can effectively be overseen and physical layer security can be enhanced. At the core are novel devices such as perovskite based diodes, gallium nitride (GaN) micro-LEDs and single photon avalanche diodes. These are inserted in optical front-ends and subsystems which incorporate versatile optics additionally the analogue circuitry to drive the LEDs and shape the signals gotten from the PDs at the recipients. In arrange to accurately demonstrate link margins, establish the coherence transfer speed of the channel and correctly model CCI, exact channel models are required which take the spectral composition of the flag into consideration [7]. Connect level algorithms are required to ideally shape the signals to maximize the information throughput. In this setting, due to the inspiration of the power signals in IM, an unused hypothetical system is needed to build up the channel capacity since the conventional Shannon framework isn't entirely pertinent [8]. New medium access control (MAC) protocols that take into consideration the unique features of the Li-Fi physical layer are necessary to enable multiuser access. To maintain fairness and good overall system performance, interference mitigation methods are also required. Finally, the optical attocell network should be incorporated into software-defined networks that are regulated by the separation of the network components. This necessitates the creation of new Li-Fi agents. There has been a lot of study into the inner two layers that characterize VLC, but there has been relatively little research into the remaining areas, such as channel modeling, where there has been a heightened interest recently.

1.1.1 Main benefits of Li-Fi

Li-Fi's indisputable benefits stem from the characteristics of light. As previously stated, it provides a highly broad and uncontrolled spectrum that may be used to produce extraordinarily high data speeds, particularly when data is sent over parallel wavelengths [32]. Simultaneously, Li-Fi offers more security than RF technologies since light beams cannot pass through barriers and may be easily bent by optical devices, reducing the danger of accidental eavesdropping. Additionally, Li-Fi may benefit from great spectrum efficiency by pushing the boundaries of spatial reuse. As with other wireless technologies, Li-Fi is based on cells formed by geographically scattered access points (AP) that provide continuous connectivity to any suitable mobile user equipment (UE). An AP's coverage is constrained by the light source's characteristics, which are governed by eye safety or lighting standards. As a result, Li-Fi cells often have diameters of a few meters, far smaller than conventional RF cells. These benefits, combined with the fact that light does not interfere with radio frequency (RF), make Li-Fi an intriguing solution for complementing and offloading the RF spectrum, as well as providing wireless connectivity in areas where RF is restricted due to electromagnetic interference or health concerns. For instance, France's 2015 "Loi Abeille" forbids the use of WiFi in sections of public businesses dedicated to the welcome, relaxation, and activities of children under the age of three [34]. Finally, one of the most recent significant concepts in Li-Fi is to leverage existing LED lighting infrastructure to offer network access, as more than 70% of traffic happens inside [33]. This manner, the rising demand for connection can be met with little additional energy consumption and without the need for new, dedicated infrastructure, making Li-Fi a ‘green' technology compatible with 6G aspirations.

1.1.2 The Li-Fi Vendors Ecosystem

In the 2010s, numerous organizations in Europe began commercializing Li-Fi technologies. Oledcomm was founded in 2012 as a spin-off from the University Paris-Saclay, following initial research on automotive VLC at the Laboratoire d'Ingénierie des Systèmes de Versailles. Following the development of the VLC and OCC product lines, Oledcomm concentrated its efforts on the creation of Li-Fi devices, which is currently its primary emphasis. In 2017, MyLi-Fi introduced the MyLi-Fi lamp, which was meant primarily as a remotely operated light treatment lamp but also included a 10 Mbps Li-Fi network connection. Then, in 2019, the Li-FiMAX solution for indoor networking was released, as seen in Figure1. Other European organizations, such as the businesses pureLi-Fi and Signify, as well as the Fraunhofer research institution, are currently offering Li-Fi solutions. pureLi-Fi was formed in 2012 as a spin-off from the University of Edinburgh and debuted the Li-Fi-XC product for indoor networking with Li-Fi-integrated lighting in 2017 in collaboration with the lighting firm Lucibel.

Figure 1. The Li-FiMAX AP and dongles

Then, in 2019, it unveiled the Gigabit Li-Fi component, a thin, light antenna that can be installed directly into mobile devices. On the other hand, Signify was formerly the lighting business section of Royal Philips, which bought the start-ups Luciom and subsequently Firefly in order to launch its TruLi-Fi range of devices in 2019. Finally, the Fraunhofer institute has a long history of research on OWC, which resulted in the Heinrich Hertz Institute (HHI) developing the Gigabit VLC module and the Institute for Photonic Microsystems developing the Li-Fi Hotspot (IPMS). Outside of Europe, Li-Fi has attracted industrial attention, with suppliers such as VLNComm in the United States and Velmeni in India. Simultaneously, numerous firms in the lighting and telecommunications industries, such as Nokia, Orange, and Ledvance, are actively monitoring the Li-Fi market's growth, despite the fact that they are not direct sellers.

1.1.3 Market Feedback and Main Li-Fi Use Cases

In the 2010s, numerous organizations in Europe began commercializing Li-Fi technologies. Oledcomm was founded in 2012 as a spin-off from the University Paris-Saclay, following initial research on automotive VLC at the Laboratoire d'Ingénierie des Systèmes de Versailles. Following the development of the VLC and OCC product lines, Oledcomm concentrated its efforts on the creation of Li-Fi devices, which is currently its primary emphasis. In 2017, MyLi-Fi introduced the MyLi-Fi lamp, which was meant primarily as a remotely operated light treatment lamp but also included a 10 Mbps Li-Fi network connection. Then, in 2019, the Li-FiMAX solution for indoor networking was released, as seen in Figure 1 and explained in Section II. Other European organizations, such as the businesses pureLi-Fi and Signify, as well as the Fraunhofer research institution, are currently offering Li-Fi solutions. pureLi-Fi was formed in 2012 as a spin-off from the University of Edinburgh and debuted the Li-Fi-XC product for indoor networking with Li-Fi-integrated lighting in 2017 in collaboration with the lighting firm Lucibel.

Then, in 2019, it unveiled the Gigabit Li-Fi component, a thin, light antenna that can be installed directly into mobile devices. On the other hand, Signify was formerly the lighting business section of Royal Philips, which bought the start-ups Luciom and subsequently Firefly in order to launch its TruLi-Fi range of devices in 2019. Finally, the Fraunhofer institute has a long history of research on OWC, which resulted in the Heinrich Hertz Institute (HHI) developing the Gigabit VLC module and the Institute for Photonic Microsystems developing the Li-Fi Hotspot (IPMS). Outside of Europe, Li-Fi has attracted industrial attention, with suppliers such as VLNComm in the United States and Velmeni in India. Simultaneously, and as discussed in Section IVE, numerous firms in the lighting and telecommunications industries, such as Nokia, Orange, and Ledvance, are actively monitoring the Li-Fi market's growth, despite the fact that they are not direct sellers.

1.2 Standardization and ecosystem development

The widespread adoption of a technology like Li-Fi is predicated on two key tenets. On the one hand, there exist standards, which are a necessary condition for widespread adoption of Li-Fi systems. On the other hand, Li-Fi manufacturers alone cannot expand the market; they must be incorporated into a wider ecosystem comprised of several companies in diverse areas. Sections below provide an overview of the different existing Li-Fi standards.

1.2.1 Early standards

After the Japan Electronics and Information Technology Industries Association (JEITA) published two initial VLC standards in 2007 – the JEITA CP-1221 and JEITA CP-1222 – standardization efforts were concentrated in 2009 within the IEEE, more precisely within its 802.15 working group, initially through task group (TG) 7. Thus, in 2011, an IEEE 802.15.7-2011 standard inspired by ZigBee is issued, increasing VLC's exposure. However, this standard is rarely maintained, which is why the TG7 began a redesign in 2015 that would result in a new mount primarily dedicated to OCC in 2018. Meanwhile, standardization efforts on Li-Fi have been centered in the IEEE 802.15.13 group from 2017 and in parallel with the IEEE 802.11bb group since 2018.

1.2.2 IEEE 802.15.13 for Industrial Applications

TG13 was formed after it became obvious that IEEE 802.15.7 could not adequately address OCC and Li-Fi. Its objective is to provide an OWC standard that enables data transfer speeds of up to 10 Gbps over a distance of 200 meters in point-to-point and point-to-multipoint configurations with wavelengths ranging from 10,000 to 190 nm. The first critical point is the definition of a primary physical (PHY) layer based on DC-biased optical orthogonal frequency division multiplexing (DCO-OFDM) with adaptive bit-power-loading, a technique derived from G.hn and designed to optimize link performance in the presence of channel variations. Additionally, a low-power PHY layer based on pulsed modulations is specified for the most resource-intensive use cases.

The other critical aspect is the inclusion of a coordinated topology at the medium access control (MAC) level, with a 'master coordinator' capable of managing multiple 'coordinators' acting as APs to the UEs. This architecture, dubbed dispersed multiple input multiple output (MIMO), is notable for its ability to enable extremely rapid handover, making it ideal for highly mobile applications like as industrial robots. A second, more conventional MAC is also established to accommodate corporate applications' less constrained mobility.

Table I. Feature comparison of the main Li-Fi standards

Standard	IEEE 802.11bb	IEEE 802.15.13	ITU G.vlc
Main target	Mass-market	Industry, enterprise	In-premise network
Peak data rate (Gbps)	5	10	2
Wavelength range (nm)	800-1000	190-10000	190-5000
Multiuser	Yes	Yes	Yes
Handover	Yes	Yes	No
Date of completion	2021	July 2020	March 2019
Chipsets	No	No	Yes

1.2.3 IEEE 802.11bb for Mass-Markets

Along with the previously described MAC layers, discussions within TG13 on this issue have resulted in the suggestion to employ the 802.11 layers. It was subsequently determined that this proposal should be included directly into 802.11, which resulted in the establishment of the TGbb in May 2018. The TGbb is designed to support Li-Fi connections with speeds ranging from 10 Mbps to 5 Gbps while still addressing the demands of the general market, particularly smartphones. It aims to make current WiFi chipsets Li-Fi compliant, therefore reusing as much of the 802.11 PHY and MAC layers as feasible.

As a result, the common PHY mode for 802.11a has been specified as the 20 MHz PHY layer. Additionally, discussions are underway to design more efficient PHY layers, including contributions inspired by 802.11ax and 802.15.13, respectively. These various PHY modes must function throughout a wavelength range of at least 800 nm to 1000 nm. Simultaneously, the TGbb will begin discussions on the MAC layers shortly. The main concept is to use a

standard 802.11 MAC to provide compatibility with existing WiFi management systems. This should enable natural changeover between WiFi and Li-Fi, as well as connectivity with the 4G/5G network management framework. As indicated in Table I, all of this work should be finished by 2021.

1.2.4 ITU G.vlc

Between 2009 and 2010, the ITU adopted a first set of recommendations for home networking called G.hn, which defines the physical layer (PHY) and data link layer (DLL) for up to 2 Gbps operation via telephone wire, coaxial cables, power lines, and plastic optical fiber. The PHY layer specified in Recommendation G.9960 was already based on DCO-OFDM, making it suitable for Li-Fi communication. As a result, the first Li-Fi demonstrations were conducted using existing G.hn chipsets, demonstrating the benefits of G.9960, particularly its bit-powerloading feature, for such applications.

The ITU launched the G.vlc project in 2018 with the goal of defining the system architecture and PHY/DLL functionality of Li-Fi transceivers for high-speed indoor networking applications. This resulted in the publishing in 2019 of a new set of PHY recommendations dubbed G.9991, which contains all of the characteristics of G.9960 but also includes an OFDM-based PHY. On the DLL side, G.vlc maintains the same Recommendation G.9961 as G.hn, ensuring that G.hn chipsets are really G.vlc-ready. It supports up to 16 users per domain (i.e. AP) through TDMA or frequency division multiple access (FDMA), but does not currently enable native handover. However, corrigendum to ITU guidelines are frequently released with new features, allowing for the appearance of this critical function and a subsequent edition of G.9961.

As seen in Table I, G.vlc is the only Li-Fi standard having commercially available chipsets. This is mirrored in the current market offerings, as Oledcomm's Li-FiMAX, Singify's TruLi-Fi, and HHI's GigabitVLC are all based on similar chipsets.

1.2.5 The Light Communication Alliance

Section II-C has already introduced several Li-Fi suppliers, as well as several other significant participants in the Li-Fi industry. The majority of these actors are members of the Light Communications Alliance (LCA), which was officially launched in December 2019 with the mission of "driving a consistent, focused, and concise approach to market education that emphasizes the benefits, use cases, and timelines for light communications" through the development of a collaboration framework involving not only Li-Fi vendors but also, among others, chipset vendors.

The LCA is organized into three working groups (WG) that each have a distinct goal. WG1 is responsible for the LCA's management and is in charge of trademarks, incorporation, membership, as well as the association's growth and marketing. WG2 is committed to marketing, namely to promoting OWC through conferences, white papers, but also by establishing real-world deployment collaborations and following the topic's newest developments. Finally, WG3 is responsible for interaction with standardization organizations such as the IEEE, the ITU, and the 3GPP, as well as with other industrial alliances such as

the WiFi Alliance and the HomeGrid Forum. The ultimate objective is to incorporate Li-Fi as a critical component of 5G and even more 6G frameworks.

1.3 Modulation techniques in Li-Fi

This section summarizes the most common digital modulation techniques used in Li-Fi, as well as certain unique difficulties and needs. In theory, Li-Fi relies on electromagnetic radiation for data transfer as well. As a result, commonly used modulation techniques in RF transmission may be used to Li-Fi with little changes.

Among Single-Carrier Modulation(SCM) schemes for Li-Fi following have been studied widely: On-Off Keying (OOK), Pulse Position Modulation and Pulse Amplitude Modulation (PAM). OOK is a well-known and straightforward modulation technique that offers a fair balance of system performance and implementation complexity. OOK can inherently provide dimming support due to the fact that it communicates data by progressively turning on and off the LED. OOK dimming can be performed by: I refining the ON/OFF levels; and ii) applying symbol compensation, as defined in IEEE 802.15.7 [9]. Dimming by refining the ON/OFF levels of the LED may retain the same data rate; however, at low dimming levels, the reliable communication range decreases. Dimming via symbol compensation, on the other hand, may be accomplished by adding extra ON/OFF pulses, the duration of which is defined by the desired dimming level. Because the maximum data rate is reached with a 50% dimming level assuming an equal number of 1 and 0 s on average, changing the brightness of the LED causes the data rate to drop.

PPM is more power-efficient than OOK but has a lower spectral efficiency. Variable pulse position modulation (VPPM)[9] is a PPM variation that can provide dimming assistance by altering the width of signal pulses in response to a defined brightness level. As a result, VPPM may be thought of as a hybrid of PPM and Pulse Width Modulation (PWM). A unique SCM technique known as optical spatial modulation [10], which is based on the spatial modulation principle, demonstrates to be both power- and bandwidth-efficient for indoor optical wireless communication. Carrier-less amplitude and phase modulation [11] is a variation of quadrature amplitude modulation (QAM) for single carrier systems that use two orthogonal signals in place of the real and imaginary parts of the QAM signaling format, for a spectrum-efficient signal transmission in Li-Fi networks.

As the necessary data rate in Li-Fi networks grows, SCM schemes like OOK, PPM, and PAM begin to suffer from undesirable consequences including non-linear signal distortion at the LED front-end and inter-symbol interference caused by frequency selectivity in dispersive optical wireless channels. As a result, multi-carrier modulation(MCM) is being pursued for high-speed optical wireless communication. MCM is more bandwidth-efficient than SCM but less energy-efficient. Orthogonal Frequency Multiplexing Modulation OFDM [12] is one, and possibly the most frequent, realization of MCM in Li-Fi networks, in which parallel data streams are broadcast concurrently through a collection of orthogonal subcarriers and complicated equalization can be avoided. If the number of orthogonal subcarriers is selected so that the modulated signal's bandwidth is less than the optical channel's coherence bandwidth, each sub-channel may be thought of as a flat fading channel. Techniques that have already been established for flat fading channels may therefore be used. The adoption

of OFDM allows for more adaptable bit and power loading strategies on each subcarrier, resulting in improved system performance.

An OFDM modulator is formed of an inverse discrete Fourier transform block, which is effectively realized using the inverse fast Fourier transform (IFFT), followed by a digital-to-analogue converter (DAC). As a result, the resulting OFDM signal is complex and bipolar in character. To fulfill the IM/DD requirements imposed by commercially available LEDs, changes to traditional OFDM methods are required for Li-Fi. The most frequent method for producing a true time-domain signal is to retain the Hermitian symmetry of the OFDM subcarriers at the price of losing half of the available bandwidth. Although this approach generates a real-time domain signal, it is bipolar and must be transformed to a unipolar signal before transmission. Adding a DC bias to the bipolar OFDM signal is the usual way of transforming it to a unipolar symbol. This is referred to as DC-offset OFDM (DCO-OFDM) [1]. The amplitude of the needed DC bias, on the other hand, is determined by the peak to average power ratio (PAPR) of the OFDM symbol, and because OFDM has a high PAPR ratio, the quantity of DC bias is substantial.

The Asymmetric Clipped Optical OFDM (ACO-OFDM) suggested in [13] does not require any DC bias. Only odd subcarriers contain information symbols in ACO-OFDM, and any negative values are clipped at the transmitter. [14] demonstrates that clipping the time domain signal does not deform symbols in odd subcarriers, despite the fact that their amplitude is scaled by half. ACO-OFDM performance is compared to that of other modulation techniques such as on-off keying and DC-biased OFDM (DC-OFDM). According to the findings, ACO-OFDM offers higher power efficiency than any other modulation method for optical wireless channels. The performance of ACO-OFDM can be increased further by employing bit loading methods. It is clear that the research community has adopted ACOOFDM as the primary unipolar OFDM method for optical wireless communication. To the best of my knowledge, an alternate unipolar OFDM method has been generally disregarded. Flip-OFDM is the term given to this method. The positive and negative portions of the bipolar OFDM real time-domain signal are extracted and sent in two successive OFDM symbols in Flip-OFDM. Both subframes have positive samples since the negative portion is reversed before transmission. As a result, flip-OFDM is a unipolar OFDM technology that may be applied in optical wireless communications.

1.4 Perovskite based diodes in Li-Fi

The main components of Li-Fi transceiver are light emitting diode(LED) and photodiode(PD); the performance of these devices are significant to determine the characteristics of whole system. Perovskite materials, with unique optical and electronic properties (such as high optical absorption), long carrier diffusion length, high carrier mobility, tunable optical bandgap, low-cost, and simple fabrication processes, have sparked significant interest in the development of high-performance perovskite-based optoelectronic devices.

The last twelve years (2009–2021) have witnessed an explosion of interest in organic–inorganic halide perovskites in the photovoltaics and light-emitting diode research groups. Furthermore, recent developments have shown that this form of perovskite has a lot of potential in the light-signal detecting technique with comparable performance to

commercially available Crystalline Si and III–V photodetectors are readily accessible and also in light-signal generation with its high photoluminescence quantum efficiency, excellent color purity and good charge mobility.

1.4.1 Perovskite based LED

In recent years, organic–inorganic perovskite-based materials have garnered considerable attention as promising materials for a variety of applications, including solar cells, light-emitting diodes (LEDs), photodetectors, and laser diodes, owing to their unique properties, which include long carrier diffusion lengths, high absorption coefficients in the visible wavelength, and high absorption coefficient [17]. However, the long-term performance of these halide perovskite-based optoelectronic devices is generally harmed by the volatilization of the organic components during the device manufacturing process,[18] the penetration of external H2O/O2, which results in device degradation,[19], and the unintentional interaction of the metal electrodes and the underlying halide perovskite [20]. Numerous effective methods have been developed to address these issues, including the reinforcement of material/interface quality,[21,22] the incorporation of a low-dimensional structure (i.e., the quantum-dot perovskite layer),[22] the use of a moisture-insensitive precursor,[23] and the modification of the electrode category,[24]. Huang et al. demonstrated the effect of the grain size of the perovskite, indicating that the surface roughness of perovskite thin films is critical for maintaining the high radiative recombination rates of MAPbBr3 perovskite LEDs (PeLEDs). [26] Due to the incompatibility of the perovskite thin film's hydrophobic/hydrophilic nature with the electron transport layer (ETL), the surface defect of perovskite thin films results in low light emission efficiency of the manufactured devices. Fullerene derivatives like as PCBM, ICBA, or C60 have been frequently utilized as the ETL in inverted-type MAPbBr3 photovoltaic devices. Not only can the fullerene derivatives act as a trap passivation layer for the perovskite thin film (e.g., the shallow (deep) traps can be passivated using a PCBM (C60) thin film), but they also considerably inhibit halide migration at grain boundaries. Additionally, the PCBM/C60 bilayer was shown to be more effective at interfacial defect passivation than the PCBM thin film alone. According to Chiu et al., phase separation between the hydrophobic PCBM molecules and the hydrophilic fullerene derivatives results in the layered structure of the resulting films, which features a hydrophilic feature at the ETL/perovskite interface and a hydrophobic surface [27].

In this project the MAPbBr3 based PeLED proposed in [26] is considered as light source in Li-Fi system, the specification of PeLED is discussed in Methods chapter

1.4.2 High sensitive perovskite photodetectors

Photodetectors, as a key component in intelligent optoelectronic systems, can transform an optical signal into an electrical signal, which has several uses. Perovskite–organic hybrid photodetectors combine the benefits of perovskite semiconductor materials (high charge carrier mobility and tunable optical bandgap) and organic semiconductor materials (facilitative solution-processing), and are thus expected to achieve special wavelength detection, exhibit superior performance, and further extend the spectral detection region. Furthermore, prospective multifunctional Perovskite Photodetectors (PePDs) have the

potential to transcend the limitations of the single functional model and satisfy the demand for variety in practical applications. Because of their low cost and weight, flexible PePDs have a wide range of applications in the realm of wearable and portable electronics.

One of the main characteristics of the Li-Fi system is its bandwidth, which is determined both by LED and PD. That is why, it is vital to use PDs with as high bandwidth as possible in future Li-Fi networks, the PePDs bandwidth measurement could be done by several methods, which were performed in the chapter below.

1.5 Machine Learning in VLC

Machine learning (ML) techniques have been effectively utilized in a variety of applications, including prediction, classification, pattern recognition, and data mining [29]. To begin, numerous useful machine learning algorithms have been demonstrated to address nonlinear issues in the optical communication field, such as estimating parameters from noise, determining the complex mapping relationship between the input and output signals, inferring the probability distribution of received signals, and estimating output values based on input samples [29,30]. Second, machine learning methods such as neural networks and K-means algorithms may be used to monitor communication performance. These algorithms can assist in estimating various channel impairments and efficiently managing optical networks [31]. Additionally, machine learning techniques like as the support vector machine (SVM) and the K-means algorithm are capable of properly identifying modulation types and bit rates. Due to the fact that machine learning algorithms can fit and model the link between inputs and outputs based on samples and labels without fully assessing the complicated relationship between each feature, ML techniques may be used to improve the transmission performance of VLC systems [28].

1.5.1 The Architecture of ML Enhanced VLC System

Fig. 2 illustrates the usual construction of an ML augmented VLC system. The complete system may be split into five functional components: a VLC transmitter, a driving circuit, a VLC channel, a reception circuit, and a VLC receiver.

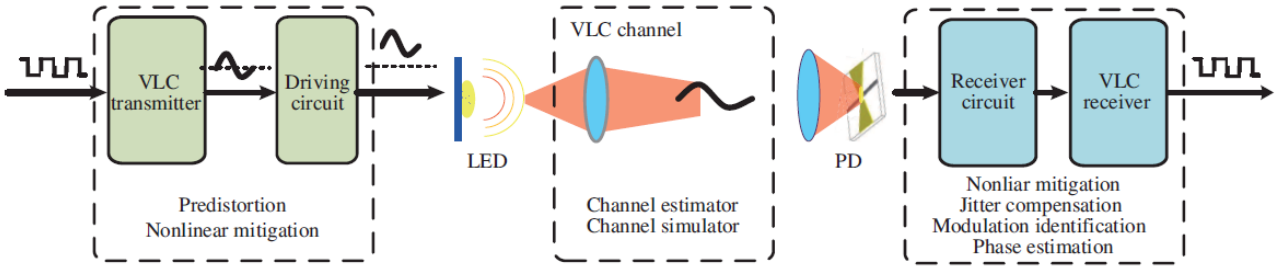

Figure 2. A machine learning enhanced VLC [28]

Typically, the transmitter and receiver are the ML-enhanced components.

The VLC transmitter performs digital signal processing operations such as encoding the transmitting binary data, modulation, pre-equalization if necessary, up conversion, and ultimately creation of the digital signal suitable for transmission to the transmitter circuit.

The driving circuit is composed of the following components: the arbitrary waveform generator (AWG), the electronic ampLi-Fier (EA), the hardware pre-equalizer, the bias tee, and, of course, the LED. The AWG completes the conversion of the produced digital signal to analogue; the hardware pre-equalizer increases the useable bandwidth of the VLC system; and the bias tee combines the bipolar zero-mean signal with the direct current bias and so powers the LED.

A VLC system's channel might be either open space or underwater. The characteristic of light attenuation in a channel is complex, causing confusion in the channel model and posing difficulties in VLC systems.

The receiver circuit collects the light with the signal, which comprises the photodiode (PD), the transimpedance amplifier (TIA), the equalization amplifier (EA), the attenuator, and the oscilloscope. Together with the EA, the TIA amplifier the feeble electrical signal generated from light by the PD. The attenuator regulates the amplitude of the amplified signal to ensure that it fits within the dynamic range of the oscilloscope, which serves as the analogue-to-digital converter.

At the receiver side, the VLC receiver performs digital signal processing via a number of operations such as differential operation, down-conversion, post-equalization, demodulation, and eventually decoding. The decoded binary data stream may be used to determine the bitwise error rate, which indicates the overall transmission system's performance.

2. METHODS

At the most fundamental level, Li-Fi systems are composed of LED transmitters that use the intensity modulation concept to transform the incoming electrical signal to information prior to transmission over the optical channel. The LED transmitter is capable of registering new users and serving multiple users concurrently over the same optical channel, therefore establishing a Li-Fi access point (AP). Photodetectors (PD) are used in the receivers to convert falling light to optical current. Many contemporary receivers are portable and equipped with the required gear for simulating the Li-Fi system's mobility and analyzing its influence on receiver gain. A precise error assessment for packet reception may be achieved using the receiver gain and the channel. The following section discusses a comprehensive mathematical description of the Li-Fi systems' fundamental components.

2.1 Perovskite diodes

Metal halide perovskites are flexible, solution-processable semiconductors that have excellent light emission and detection properties [36-41]. Perovskite LEDs, for example, have exhibited external quantum efficiencies (EQEs) in excess of 20% [43-45], while perovskite photodetectors have showed a low detection limit of $sub - pW\ cm^{-2}$, as well as nanosecond response times [40-42]. These advancements, along with the low Stokes shift of perovskite materials, imply the possibility of developing high-performance solution-processable dual-functional perovskite diodes that can act as both an optical transmitter and receiver for wireless optical communications.

2.1.1 Perovskite LED

As a transmitter, PeLED, designed by [35], was considered in this work, and the PeLED characteristics were based on the measurements results obtained by [35]. The PeLEDs were made of an indium tin oxide (ITO)-coated glass/polyethylenimine ethoxylated (PEIE)-modified zinc oxide (ZnO)/formamidinium lead iodide perovskite (50 nm) device structure. /poly(9,9-dioctylfluorene-co-N-(4-butylphenyl)diphenylamine) (TFB) (40 nm)/molybdenum oxide (MoOx) (70 nm)/gold (Au) (80 nm (Fig. 2). To reduce defects in the perovskite layer, an effective passivation agent called 2,2′-(oxybis(ethylenoxy))diethylamine (ODEA) created in 47 was utilized. As seen in Fig. 3 b, when the diode operates at a positive bias greater than the turn-on voltage, electrons and holes are fed into the perovskite emitters, where they undergo effective radiative recombination to create light. The optimized perovskite diode (passivated with 30% ODEA and a precursor concentration of 0.13 M) exhibits optimal electroluminescence (EL).

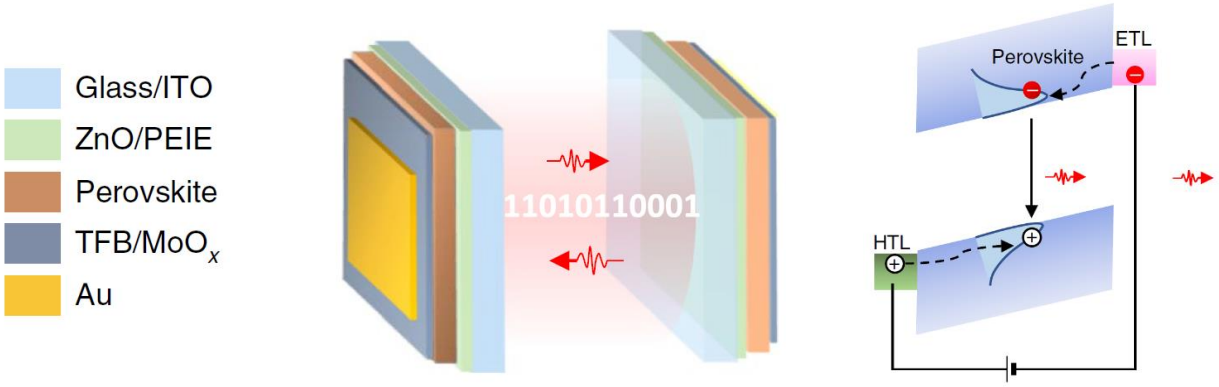

a b

Figure 3. Schematic illustration of PeLEDs. a, Schematics of using perovskite diodes for inter- (left) and intra- (right) chip data communications. b, Schematics of the energy diagram of the perovskite diode under forward bias as an LED [35].

The authors initially exhibited the perovskite diodes' outstanding performance and rapid reaction time as LEDs. The characterization findings indicate a low turn-on voltage of 1.3 V and a maximum radiance of 314 W sr1 m2 (Fig. 3a). The maximal EQE value of 21.2 percent is among the highest observed for perovskite LEDs [43-47]. Devices' excellent EL performance is primarily due to the efficient passivation of ODEA to the iodide vacancy on the perovskite crystal surfaces, which was previously studied in detail [47].

To characterize the response speed, the evolution of the EL intensity and current of square-wave-driven diodes were observed (Fig. 3b). At a low frequency of 100 Hz, both the EL intensity and current changes in lockstep with the driving voltage change. At a higher frequency of 100 kHz, a little lag between the EL intensity and the voltage change can be noticed, as well as noticeable current overshoots, which may be caused by the parasitic capacitance's charging and discharging effects.

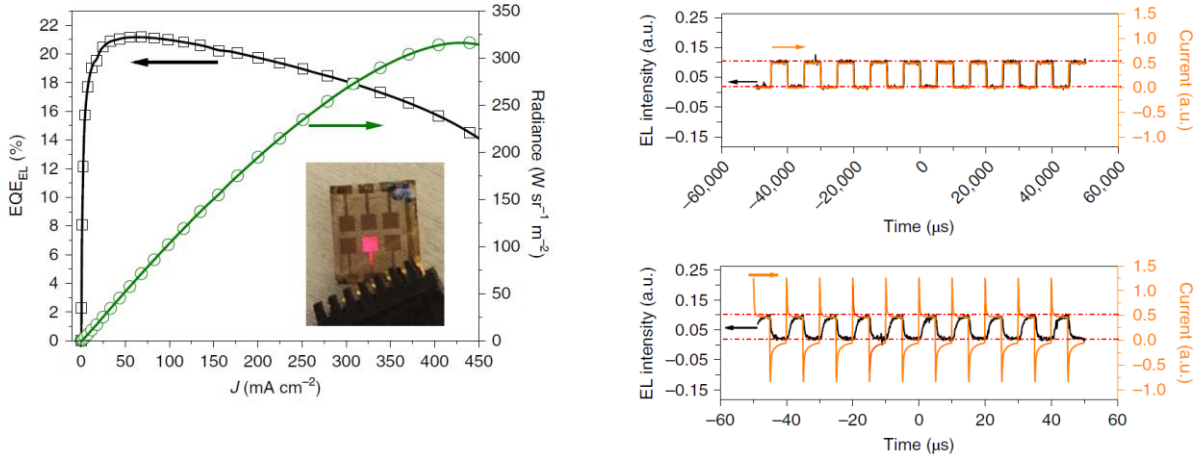

a b

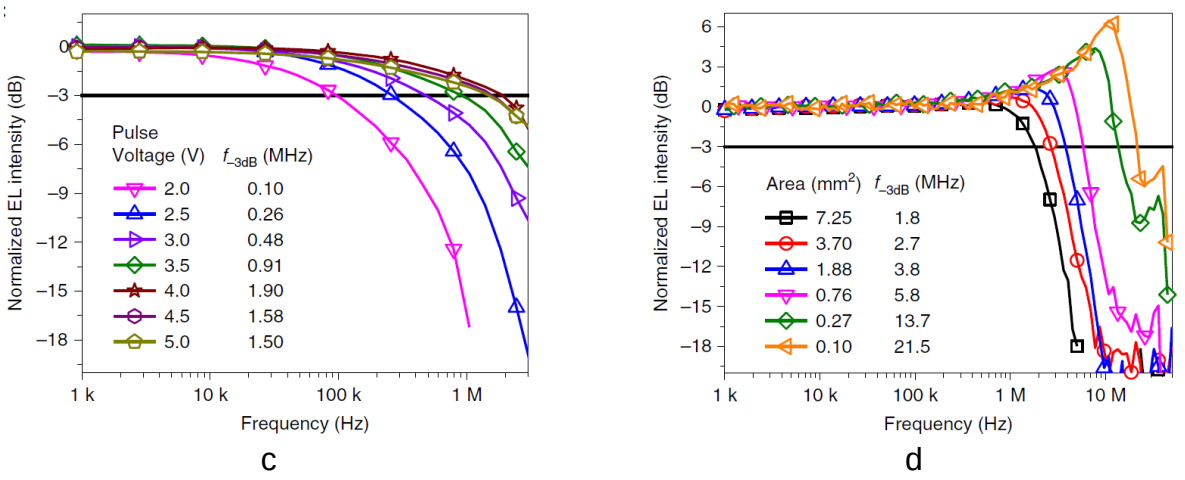

Figure 4. Characterization of PeLEDs. a, EQE and radiance versus current density curves of the optimized perovskite LEDs. Inset: photograph of the LED driven by a 3.0 V bias. b, Transient EL intensity and current characterization of the perovskite LEDs at 100 Hz (top) and 100 kHz (bottom). c, Frequency response curves of the perovskite LED under different drive pulse voltages. d, Frequency response of perovskite LEDs with different device areas [35].

To verify this, the transient current curves with an exponential function were fitted and determined that the charging and discharging processes have time constants of 120 and 172 ns, respectively (Fig. 4a). Using a serially linked resistance (5Ω), the capacitance of the device is calculated to be 2.9±0.5 nF. This estimated value is consistent with the measured value, indicating that the device's parasitic capacitance restricts the response speed when used as an LED. Notably, passivation of trap states can increase not only EL efficiency but also parasitic capacitance, therefore increasing response speed. Additionally, the EL frequency response of the perovskite diode was evaluated when it was operated at various voltages to establish the device's cutoff frequency. As seen in Fig. 4c, the cutoff frequency increases as the driving voltage increases, reaching a maximum of 1.90 MHz at 4.0 V. Increased cutoff frequency can be ascribed to quicker charge injection at a higher driving voltage, similar to what is found in inorganic and organic diodes [48-50].

The following characteristics of PeLED were used in the Li-Fi system, Table 2.

Table 2. Parameters of PeLED [35]

	Symbol	Value	Unit
Bandwidth	f_{3dB}, MHz	1.8	MHz
PeLED surface	$A_{LED}, \mu m$	7.25	μm
Angle at half-power	θ	$\frac{\pi}{3}$	$degree$
Solid angle	Ω	$2\pi(1-\cos(\theta))$	sr
Radiance	L_e	Figure 3a	$Wsr^{-1}m^{-2}$
Radiated power	ϕ_e	$\Omega A_{\mathrm{LED}} L_e$	W

2.1.2 Perovskite PD

Photodetectors have attracted considerable attention and have been utilized in a variety of sectors, including industrial production, military affairs, biochemical detection, optical communication, and scientific study.

The adaptability and availability of photodetectors are always determined by a few key factors: photoresponse speed, sensitivity to low-light conditions, the detection band in which photodetectors can detect light efficiently, and dynamic range response. The reaction time or speed, spectral responsivity (R), noise current, external quantum efficiency (EQE), specific detectivity ($D*$), and linear dynamic range (LDR) of the photodetector are the essential photodetector characteristics that should be utilized to assess these performance factors. Recently, research into high-performance perovskite photodetectors has been a focal point of attention in the fields of optoelectronics and high-quality imaging.

$$R = \frac{e\eta_{EQE}\lambda}{hc} \quad (1)$$

$$where\ e - electron\ charge, \eta_{EQE} - EQE\ coefficient, \lambda - wavelength, h - Planc\ constant,$$

$$c - speed\ of\ light.$$

Then the received electrical current can be obtained thought received optical power P_{rec} and PePD responsivity:

$$I_{rec} = P_{rec}R \quad (2)$$

The total noise (Equation 1) of PePD expressed by the sum of thermal noise, shot noise and dark current noise variances by following equations

$$\sigma_{total}^2 = \sigma_{thermal}^2 + \sigma_{shot}^2 + \sigma_{dark}^2 \quad (3)$$

The thermal noise variance of PePD with resistance $R_{load} = 50\ Ohm$, at room temperature $T = 300K$ is a Gaussian random process with zero mean. The bandwidth is considered to be half of sampling frequency of the system due to the Nyquist theorem, and we considered double sided power spectral density, that is why the bandwidth is at the range between $-\frac{f_{samp}}{2}; \frac{f_{samp}}{2}$.

$$\sigma_{thermal}^2 = \frac{2k_BT}{R_{load}}B_e, where\ k_B - Boltzman's\ constant, B - electrical\ bandwidth \quad (4)$$

The shot noise variance is a white noise and in the limits set by the Nyquist theorem:

$$\sigma_{shot}^2 = eI_{rec}B_e, (5)$$

The dark current noise variance is also a Gaussian with zero mean, is caused by dark current ,which is unwanted current or signal in a photodetector in the absence of incident light, resulting from thermally excited electrons or leakage of current along the current path.

$$\sigma_{dark}^2 = eI_{dark}B_e \ (6)$$

The PePD, which was considered in this work is from PeroCUBE project and its characteristics were taken from the data provided by Eulambia Advanced Technologies ltd. However, a number of measurements were performed in order to determine the operational bandwidth of PePDs from PeroCUBE project.

2.1.3 PePD bandwidth measurements

All measurements were taken in the Optical Communications Laboratory of National and Kapodistrian University of Athens under supervision of Dr.Kazazis and Dr.Raptis. The input signal generator is Tektronix AFG1062 with 60MHz bandwidth, 2 output channels, 1 mVpp to 10 Vpp output amplitude across full bandwidth and the oscilloscope is Tektronix TBS 1052B-EDU Digital oscilloscope, which is used to collect all measured data (one record consist of 2500 points) and its bandwidth is 150MHz. There were two light sources in our setup: OSRAM PLT5 510 (green laser diode) and ROHM RLD63NPC5 (red laser diode), Table 3-4 describes light sources specifications. According to the specifications of devices in the system design there is not limiting any factor for measurement of photodiodes bandwidth.

Table 3. Characteristics of OSRAM PLT5 510 [52]

	Symbol	Value	Unit
Output power	P_{opt}	10	mW
Operating current	I_{op}	typ. 45 max. 75	mA
Operating voltage	V_{op}	typ. 5.0 max. 6.6	V
Peak wavelength	λ_{peak}	min. 510 typ. 515 max. 530	nm
Spectral bandwidth (FWHM)	$\Delta\lambda$	typ. 2	nm

Table 4. Characteristics of ROHM RLD64NPC5 [53]

	Symbol	Value	Unit
Output power	P_{opt}	6	mW
Operating current	I_{op}	typ. 24 max. 35	mA
Operating voltage	V_{op}	typ. 2.2 max. 2.7	V
Peak wavelength	λ_{peak}	min. 630 typ. 635 max. 645	nm
PinPD Reverse Voltage	V_r	max. 20	V

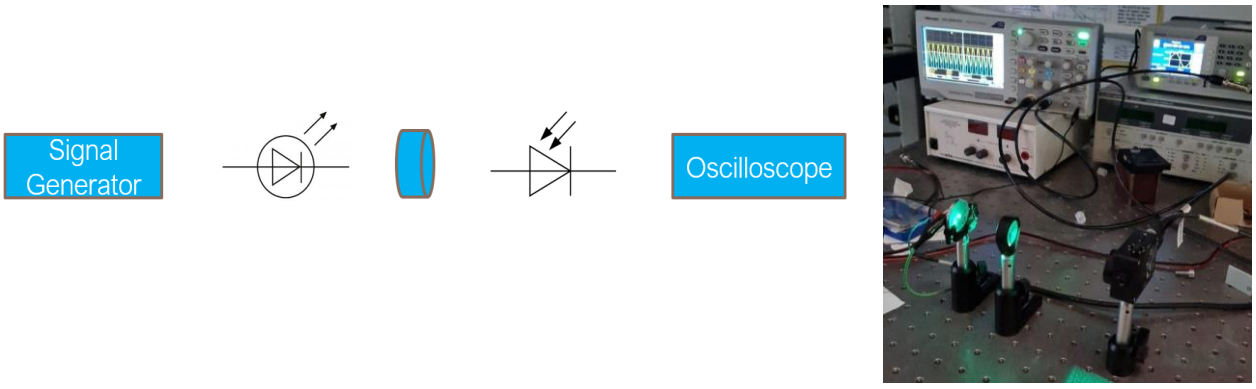

a b

Figure 5. a, PePD bandwidth measurements design. b, The bandwidth measurement process using OSRAM PLT5 510 laser as a source and ThorLabs PDA25K-EC as a detector.

The starting stage of the measurement was check if there are any limiting devices in system setup in term of frequency response. The system was validated by measuring reference photodiode ThorLabs PDA25K-EC, which is operating in the range of 150-550 nm and its bandwidth is 7.5Mhz. The PDA25K(-EC) is an amplified, switchable-gain Gallium Phosphide (GaP) detector designed to detect light signals with a wavelength range of 150–550 nm. The user may adjust the gain in ten-dB levels through an eight-position rotary switch. A buffered output drives 50 Ω load impedances up to 5 V. The PDA25K(-EC) incorporates a low-noise, low-offset, high-gain transimpedance amplifier with a gain control range of 70 dB. Adjust the gain by twisting the gain control knob on the unit's top side. There are eight gain settings, each raised by ten decibels. It is critical to keep in mind that as the gain increases, the bandwidth decreases [51].

Table 5 Specifications of reference PD PDA25K-EC [51]

	Symbol	Value	Unit
Detector	-	GaP PIN	
Active Area	-	2.2 x 2.2 (4.8 mm^2)	mm
Wavelength Range	λ	150 to 550	nm
Peak Wavelength	λ_p	440 (Typ.)	nm
Peak Response	$\Re(\lambda_p)$	0.12 (Typ.)	A/W
Amplifier GBP	-	25	MHz
Output Impedance	-	50	Ω
Max Output Current	I_{OUT}	100	mA
Load Impedance	-	50 to Hi-Z	Ω
Gain Adjustment Range	-	0 to 70	dB
Gain Steps	-	8 x 10 Steps	dB
Output Voltage	V_{OUT}	0 to 5 (50 Ω) 0 ot 10 (Hi-Z)	V

The measurement of PDA25K-EC was done by step-by-step increasing the input signal frequency and there were four measurements with following PD amplifier values: 0dB; 10dB; 20dB; 40dB. The calculation of the 3dB bandwidth f_{3dB} done by (Equation 7)

$$f_{3dB} = f_r \ \ if 10\log(V_{r.max}^2) - 10\log(V_r^2) = 3dB \quad (7)$$

,where $V_{r.max}$ is maximum received Amplitude, V_r is received Amplitude in certain input signal frequency f_r

The photodetector can be considered as a low pass filter with frequency response:

$$|H(f)|^2 = \frac{1}{1 + \left(\frac{f}{f_{3dB}}\right)^2} \ (8)$$

The source of the input signal is OSRAM PLT5 510 operating in 515nm wavelength and the input signal parameters are same for all values of amplifier and equal to: offset is 6.5V and amplitude is 1V. The results of the measurements proofs, that the system design is valid for the relevant bandwidth measurement of PePDs, since the result of measurements are close enough to the reference values from the datasheet of PDA25-EC, Table 6.

Table 6. Reference commercial PD measurement results

Amplitude, $\boldsymbol{dB}$	Measured Bandwidth, $\boldsymbol{MHz}$	Reference Bandwidth, $\boldsymbol{MHz}$
0	7.75	7.5
10	3.65	3.5
20	1.55	1
40	0.255	0.1

There are 3 methods of PD bandwidth calculations via following measurements were considered:

- Peak voltage measurement - The measurement is done by increasing the input signal frequency step by step until we reached the 3dB frequency and kept going on further till reaching fluctuations due to system design.
- Rise time measurement - For the same setup we measured high, low, peak to peak Voltage values. The input signal is pulse signal, and its offset and amplitude differ for each PePD measurement and the frequency is also kept different. From obtained voltage values we can find 10% an 90% pulse rise time and get t_{rise}, then f_{3dB} can be calculated by Equation 9.

$$f_{3dB} \approx 0.35/\mathrm{t_{rise}} \ (9)$$

- Fast Fourier Transform (FFT) measurement – the input signal is pulsed signal with certain duty cycle and frequency. The saved data points are output of FFT function of the oscilloscope.

There were 4 different PePD bandwidth to be measured by above-described methods and their specification are described in Table 6. PePDs can be categorized by their surface size and the measurements analysis shows clear difference in the performance of PePDs.

Table 7. Characteristics of PePDs

PePDs	Surface, mm^2	Peak wavelength, nm	Illumination	$J_{sc}, mA/cm^2$	V_{oc}, mV	$J_{dr}, mA/cm^2$
PePD 3 small	107	540	Light	18.66001	1014.75	1.871106
PePD 4 small	107	540	Light	17.64519	965.4591	1.959539
PePD 2 large	1460	540	Light	3.4717	5438.245	0.4021
PePD 3 large	1460	590	Light	3.4616	5482.885	0.4113

It can be noticed that the characteristics of PePD3 small and PePD4 small are relatively similar, whereas PePD2 large and PePD3 large also have same performance both in $J_{sc}\ vs\ V_{oc}$ and EQE vs wavelength relationship. From Figure 6, it can be seen that the EQE of large PePDs at the range of 520 – 600 nm are showing promising ~96% and small PePDs reaches their peak EQE values ~90% at the range of 505-530nm.

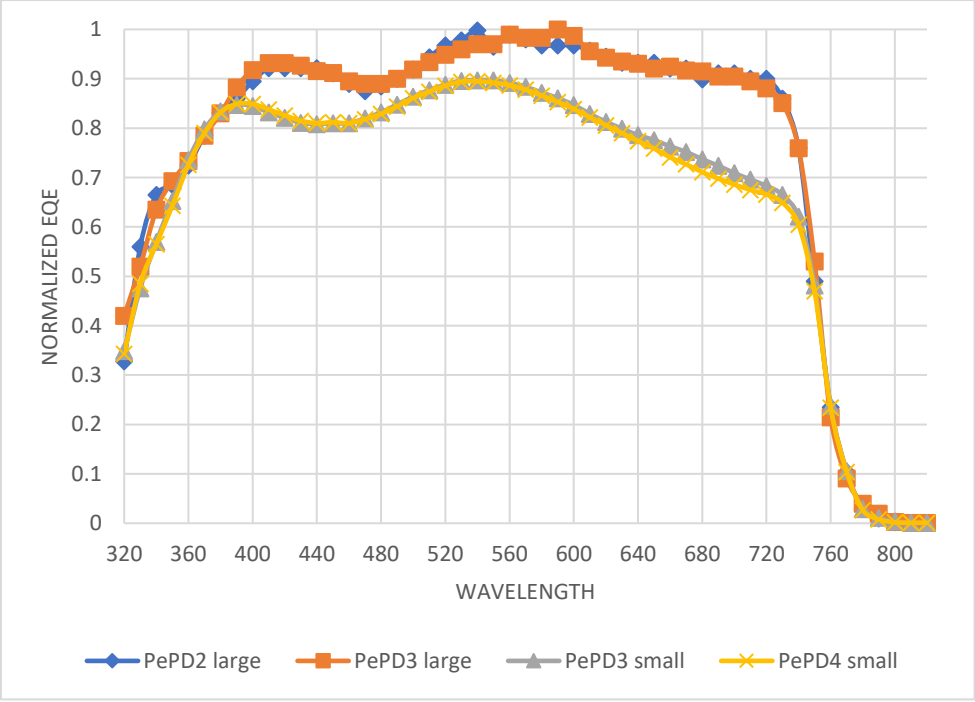

Figure 6. EQE versus wavelength relationship of PePDs

The bandwidth measurement of all four PePDs starts from Peak voltage measurement using two lasers mentioned above. Input signal parameters as offset and amplitude are kept same

per laser. For OSRAM PLT5 510 (green laser), the offset was equal to 6.4V and the amplitude was equal to 220mVpp (peak-to-peak) and for ROHM RLD64NPC5 the offset was set at 4.3V and the amplitude was 300mVpp. The Figure 6 shows the plots of ideal conventional RC filter and PePD4 small Peak voltage measurements data, it can be seen from Appendix II, that all PePDs are acting like a RC filter as well as LED.

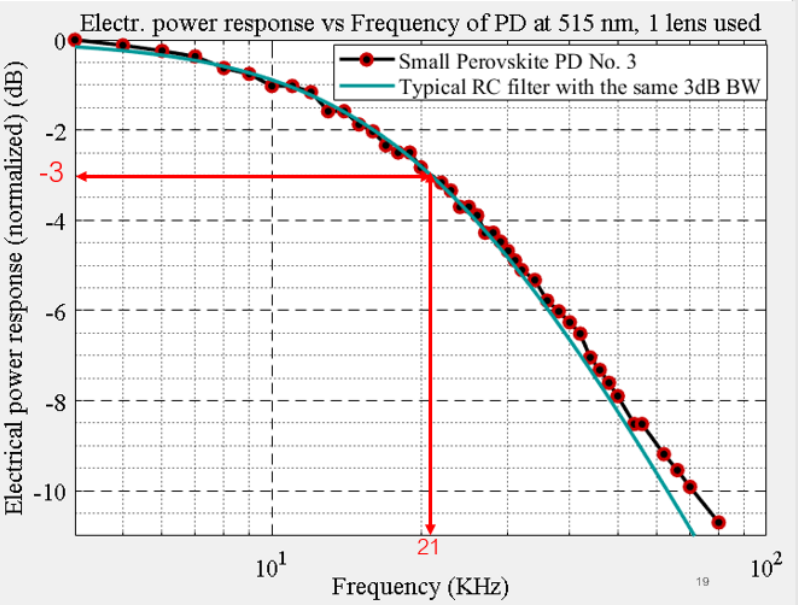

Figure 7. Electrical power response vs Frequency of PePD3 small at 515nm.

PePDs bandwidth measurement thought its response speed by using Equation (9). In general, the rise time is defined as the time for the photocurrent to increase from 10% to 90% of the peak when photocurrent arrives at a stable state after accepting illumination. This type of measurement is considered as an estimation of bandwidth. The input signal was a pulsed electrical signal with following parameters offset and amplitude, which were same as for Peak voltage measurement, except frequency, which was a fixed value for each PePD. From Figure 7b, it can be seen that measured rise is equals to the $t_{rise} = 14.8\,\mu s$, using Equation 2, we will estimate 19kHz bandwidth for PePD3 small.

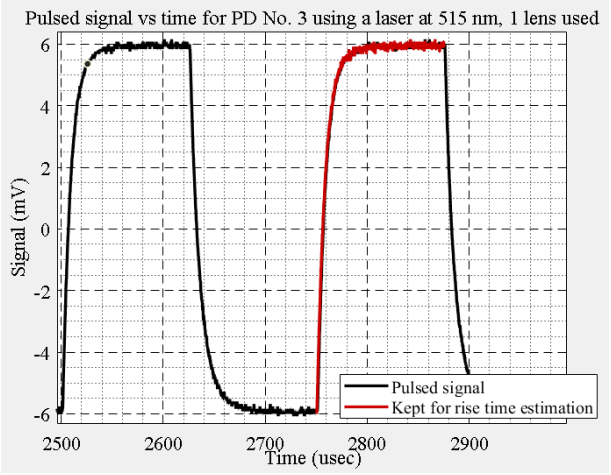

a

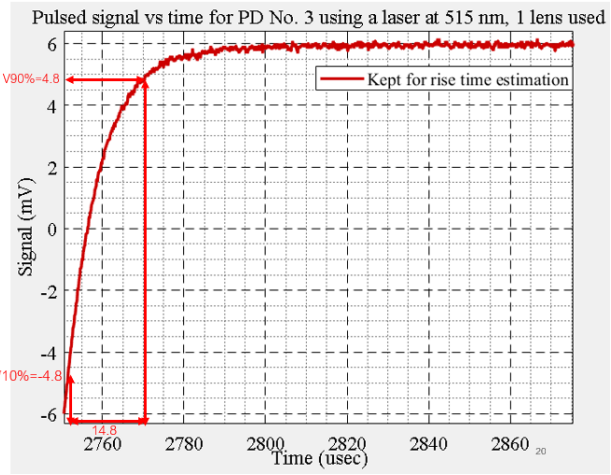

b

Figure 8. Rise time measurement of pulsed signal of PePD3 small at 515nm

A fast Fourier transform (FFT) is a mathematical operation that computes a sequence's discrete Fourier transform (DFT) or its inverse (IDFT). Fourier analysis is a mathematical technique that transforms a signal from its native domain (typically time or space) to a frequency domain representation and vice versa. The DFT is generated by decomposing a series of values into frequency-dependent components. The usage of FFT to estimate PePDs bandwidth is another approach. The input is pulsed electrical signal with duty cycle, which is 1% for small PePDs and 0.1% for large PePDs, other parameters as offset and amplitude were kept same as for rise time measurement. Figure 9. Shows the output of measurement analysis, where FFT, electrical power response of PePD3 small can be compared, the input signal pulse duration is 2.5μs and frequency is 4kHz.

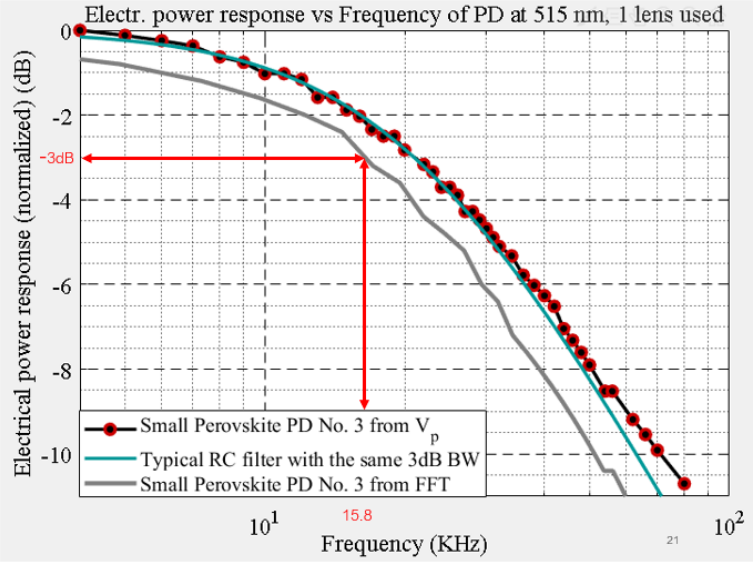

Figure 9. FFT and Electrical power response of PePD3 small at 515nm

The detailed analysis of the measurements are done in the following chapter as well as comparison of the results and consideration of the certain PePD in the Li-Fi system according to the maximum measured bandwidth.

2.2 Channel model design

To develop, construct, and operate effective optical communication systems, it is critical to have a firm grasp on the channel's properties. The channel impulse response is used to characterize a communication channel, which is subsequently used to analyze and battle the impacts of channel distortions. There has been a substantial amount of work published on channel characterization, which includes both experimental measurement and computer modeling of indoor and outdoor systems.

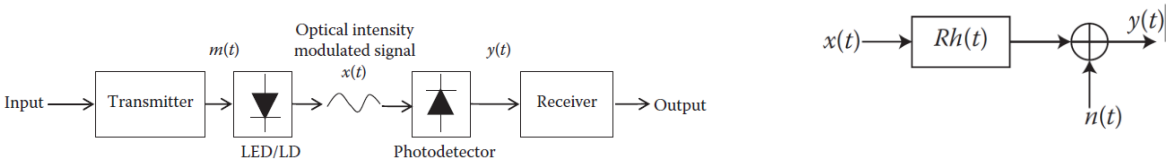

a b

Figure 10. Baseband equivalent model of a VLC employing IM/DD

The modulating signal m(t) directly modulates the driving current of an optical source, therefore varying the optical source's intensity x(t) (Figure 10a). The receiver utilizes a photodetector, which creates a photocurrent y(t) by integrating tens of thousands of extremely small wavelengths of the incident optical signal x(t). This photocurrent is exactly proportional to the incoming optical power, or to the square of the received electric field. An optical wireless system based on IM/DD has an analogous baseband model that conceals the optical carrier's high frequency nature. The model is illustrated in Figure 10b, where R denotes the photodetector response, h(t) denotes the baseband channel impulse response, and n(t) is the signal-independent noises like: shot noise, thermal noise, dark current noise.

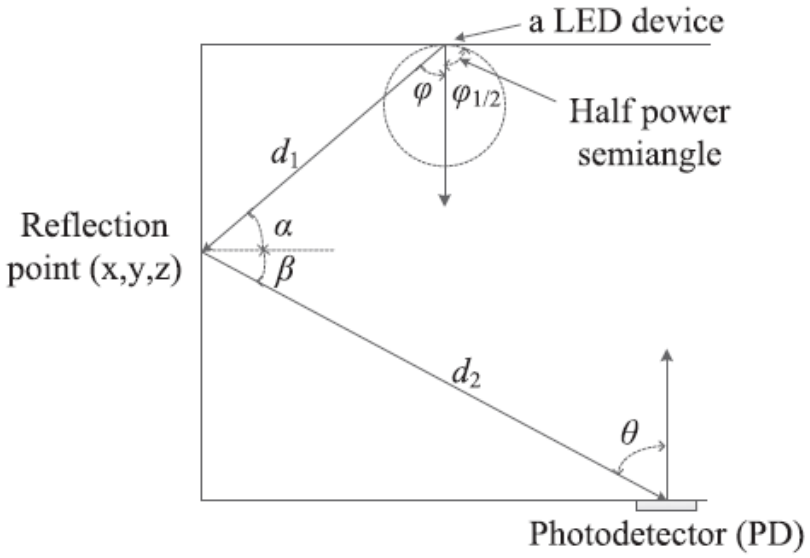

Figure 11. LoS and first-order NLoS paths of the Li-Fi channel [54]

Following that, let us examine the characteristics of optical signal power at the receiver. The direct current (DC) gain of a VLC channel is represented as in a VLC system.

$$H_{los} = \begin{cases} \frac{(m+1)A}{2\pi d^2} cos^m(\varphi) T_s(\theta)\, g(\theta) \cos(\theta)\,, & 0 \le \theta \le \psi_c \\ 0, & \theta > \psi_c \end{cases} \quad (10)$$

where Adefines the physical area of a PePD, d denotes the distance between a transmitter and a receiver, m signifies the lambert index (Equation 11),φ denotes the angle between the direction of light emission and the normal direction of the light source (the irradiance angle), and θ is the incidence angle of radiation. $T_s(\theta)$ is the gain of an optical filter, $g(\theta)$ is the gain of an optical concentrator, and ψ_c is the receiver's field of view. (FOV). m is the order of Lambertian emission which is related to the LED semi angle at half power $\varphi_{1/2}$ as given by:

$$m = -\frac{ln2}{\ln(\cos(\varphi_{1/2})} \quad (11)$$

Non-LOS connections, particularly those used in indoor applications, are vulnerable to the same consequences of multipath propagation as RF systems, although to a greater extent. Due to multipath propagation, the electric field experiences significant amplitude fades on a wavelength scale. Multipath fading would occur in the detector.

The channel DC gain of the first reflection is shown as:

$$H_{nlos} = \begin{cases} \frac{(m+1)A}{2\pi d_1^2 d_2^2} \rho dA_{wall} \cos^m(\varphi) \cos(\alpha) \cos(\beta) T_s(\theta)\, g(\theta) \cos(\theta), & 0 \le \theta \le \psi_c \\ 0, & \theta > \psi_c \end{cases} \quad (12)$$

where d_1 represents the distance between the LED and the reflection point, d_2 denotes the distance between the reflection point and the receiver, and ρ signifies the reflection coefficient, dA_{wall} signifies the emission area of a micro surface, φ denotes the radiation angle of reflection points, α expresses the incidence angle of reflection points, β denotes the receiver's radiation angle, and denotes the receiver's incidence angle.

2.2.1 The properties of indoor environment

At the moment, Li-Fi systems are mostly used in an indoor setting, where their channel models are influenced by a variety of factors, including the design of the light source, the location of receivers, the geometry of the space, and the effect of various reflectors. This section will examine the room model, and interior environment reflection characteristics. Typically, the room model is denoted by the L, H, W, where L is the length, W represents the breadth, and H represents the height. Length and breadth were typically identical in the majority of trials [53].

In the system we considered room dimensions are 3mx3mx3m, which means it's a cube and we have used 4 PeLED-arrays in the following locations (Table 8). The refractive index of walls is equal to the reflectance of the white concrete 0.4, the refractive index of pine wood door is 0.9 and window has a 0.51 reflectance (Figure 12).

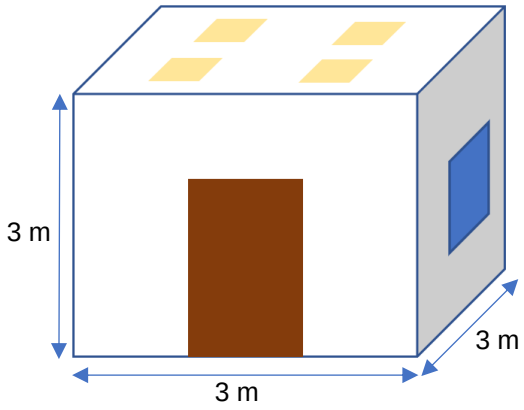

Figure 12. Visualization of the room design

Table 8. PeLED arrays location

LED array	Length, m	Width, m	Height, m
PeLED array 1	1	1	1.25
PeLED array 2	-1	1	1.25
PeLED array 3	-1	-1	1.25
PeLED array 4	1	-1	1.25

2.3 The modulation technique used in the Li-Fi system

Asymmetric clipped optical OFDM (ACO-OFDM) is a unipolar OFDM technique for optical wireless communications and was widely studied in the literature, but according to the [55] another unipolar Flip-OFDM technique provides same performance and different complexities. Flip-OFDM, in instance, offers a 50% reduction in hardware complexity over ACO-OFDM at the receiver for slow fading channels. This is the one of the main reasons, why Flip-OFDM is implemented in this Li-Fi system.

The 16 QAM modulation is used to map datapoint before IFFT block from Figure2a.

And the input to the Inverse Fast Fourier Transform (Block) is 16-QAM symbol X_k, the number subcarriers are 1024, which equal to the size of IFFT block.

$$x(k) = X_0 + \sum_{n=1}^{N/2-1} X_n \exp\left(\frac{2j\pi nk}{N}\right) + X_{\frac{N}{2}} \exp(j\pi k) + \sum_{n=N/2+1}^{N-1} X_{N-n}^{*} \exp(j2\pi nk) \qquad (13)$$

To avoid any DC shift or any residual complex component in the time domain, the X_0 and $X_{N/2}$ are set to zero. Flip-OFDM uses half of subcarriers to transmit data, so the output of IFFT block is $x(k) = x^{+}(k) + x^{-}(k)$, where positive and negative parts are defined as,

$$x^{+}(k) = \begin{cases} x(k)\ if\ x(k) \geq 0 \\ 0\ otherwise \end{cases}$$
$$x^{-}(k) = \begin{cases} x(k)\ if\ x(k) < 0 \\ 0\ otherwise \end{cases} \qquad (14)$$

Having 1024 subcarriers in total and subtracting 2 of them to avoid DC shift leads us to have 1022 subcarriers, where half of them 511 are used to transmit data.

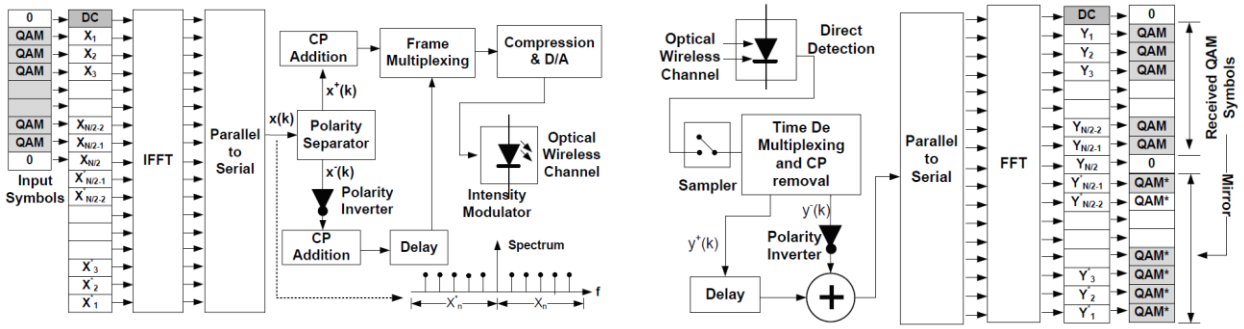

Figure 13. Block diagram of Flip-OFDM transmitter (a) and receiver (b) [55]

The positive signal $x^{+}(k)$ is sent in the first OFDM subframe, while the flipped (inverted polarity) signal $-x^{-}(k)$ is transmitted in the second OFDM subframe, as illustrated in Fig. 13a. Due to the dispersive nature of the optical channel used for transmission, both OFDM subframes are prefixed with duration Δ of cyclic prefixes. Following that, the second OFDM subframe is delayed by $(N + \Delta)$ and time multiplexed with the first (Figure 14). Both subframes contain just unipolar OFDM symbols.

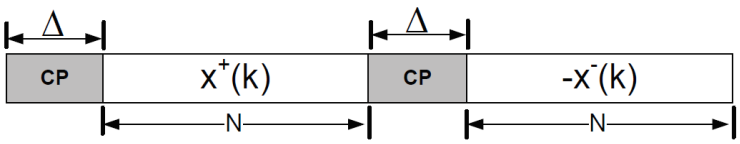

Figure 14. Flip-OFDM unipolar frame [55]

The two received subframes are used to reconstruct the bipolar OFDM frame at the Flip-OFDM receiver, as illustrated in Fig. 13b. After removing the cyclic prefixes associated with each OFDM subframe, the original bipolar signal is regenerated as, where $y^{+}(k)$ and $y^{-}(k)$ denote the first and second subframe time samples, respectively. Fast Fourier Transform (FFT) operations are used to recreate the bipolar signal in order for the receiver to detect the transmitted data symbols.

2.4 Applying Deep Learning to reduce nonlinearities at the receiver.

Deep learning (DL), a type of machine learning technique based on neural networks (NN), has lately regained great momentum following the achievement of ground-breaking performance in computer vision, natural language processing, and automated speech recognition. Additionally, a Multi Layer Perception (MLP) has been implemented in wireless physical layer communications, MLP is a class of supervised feedforward Deep Neural Networks (DNN) ,

In comparison to conventional OFDM, the decoder at the receiver uses received signals after FFT block to mitigate nonlinearities caused by the LED nonlinearities primarily stems from the Electrical-Optical conversation, PD total noise influence and channel response. The proposed algorithm consists of the dense layers, normalization and activation functions. Additionally, the dropout layer may be used after the dense layer to solve the over-fitting problem and improve the MLP model's generalization capacity, particularly when the number of sub-layers and hyper-parameters is quite big. It should be noted that the Dl model layers are trained concurrently with the IM/DD channel, and that different numbers of neurons can be used in different sub-layers to reduce network complexity.

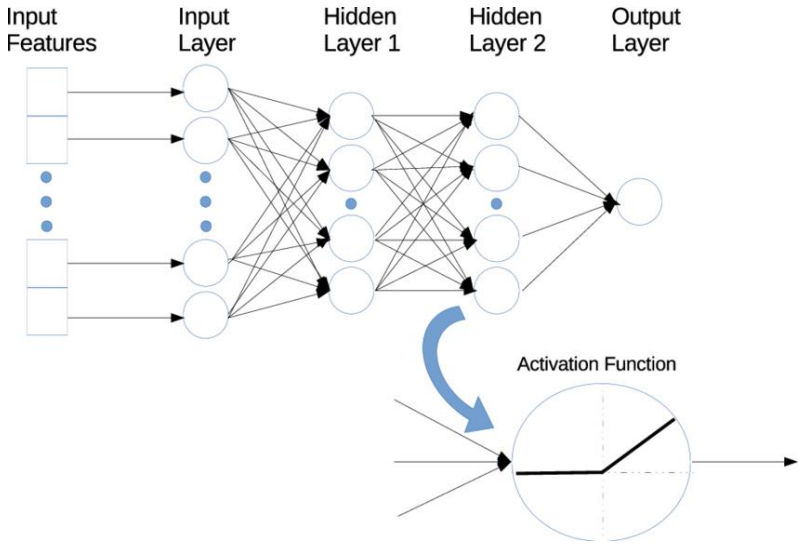

Figure 15. MLP consistion of 2 hidden layers

2.4.1 The dataset preparation

The output of 16-QAM modulation is considered as a labels t, while the output of FFT block at the receiver is chosen as a noisy dataset, which has a size of N = 51100 data points. The since our dataset represented by complex numbers, the primary task was to split real and imaginary parts of each datapoints both for labels and for the noisy dataset. As a result, dataset became a (51100,2) matrix, where real and imaginary parts of datapoints are features. In order to have larger dataset, feature extraction was done by adding the absolute of the datapoint, the square of both real and imaginary parts, which provided 3 more features and concatenation of all features transferred noisy dataset into the matrix with size of $\mathcal{P}$ = (51100,5).

Model architecture

As a DNN the MLP was used, which consists of k – hidden layers and single input and output layers, meaning the whole model will have $k + 2$ layers in total, Figure 15. As a hidden layers Dense fully connected layers are used with activation function Sigmoid. Let $\mathcal{D}_l$ denotes the number of neurons of the l –th layer, then t_l – is the input to the l-th dense layer, then the outputs can be expressed by Equation 16.

$$h_l = W_l t_l + b_l \quad (15)$$

Where $W_l \in \mathbb{R}^{\mathcal{D}_l x \mathcal{P}}$ and $b_l \in \mathbb{R}^{\mathcal{D}_l}$ are the weight matrix and bias vector for the l-th dense layer, respectively. Then, h_l l goes via the normalization unit, which normalizes the activation function's input and maintains the same distribution for each sub-input layer's during MLP training. The batch normalizing technique is used in this work, and the related outputs may be computed as:

$$(h_l)_{Bat} = \frac{\alpha_l (h_l - \mathbb{E}\{h_l\})}{\sqrt{\sigma_{h_l}^2 + \zeta}} + \beta_l \quad (16)$$

Where $(.)_{Bat}$ denotes the output of Batch normalization, α_l and β_l are the scaling and shift factors, respectively. Additionally,ζ is always set to a value near to zero to avoid the denominator becoming zero. Notably, the proper α_l and β_l can also be learnt during the training phase. The $(h_l)_{Bat}$ Bat is then sent into the activation function ρ_l, which generates the outputs of the l-th sub-layer.

If $(h_l)_{Bat}$ is a positive real value, then the Sigmoid activation function creates the same values as the $(h_l)_{Bat}$. But beyond that, linear activation is utilized for the final sub-layer since the primary purpose of the MLP net's outputs is to generate I-Q samples from the learnt dataset. The output layer uses Tanh activation function and the result is predicted dataset $t\hat{} \in \mathbb{R}^{2N}$, which is divided into two parts according to their odd and even index, and later concatenate them into complex I-Q symbol.

$$t\hat{} = \varphi_{\mathcal{L}}\{(W_{\mathcal{L}} t_{\mathcal{L}} + b_{\mathcal{L}})_{Bat}\} \quad (17)$$

Where $\mathcal{L}$ is number of dense layers in DNN.

2.4.2 DNN training

During the training stage, the proposed DNN is tuned to maximize end-to-end performance by adjusting the parameters $\Theta = \{W, b\}$ to bring the reconstruction t^ closer to the raw t. The relationship between t and t^ can be quantified using the mean square error (MSE), as given by

$$MSE(t, t^{\wedge}) = |t - t|_2^2 \quad (18)$$

While alternative loss functions were considered, they did not give any discernible improvements over the MSE.

The Adam stochastic algorithm was chosen as a traditional optimization method. The maximum number of training epochs utilized in the DNNs applications is 100, and the accuracy was computed after each training epoch using a dataset produced independently. To avoid overfitting and to remove the possibility of data sequences being periodic, the complete dataset contain is split into two subsets: training, testing by stratified K-fold with number of splits equal to 10, enabled shuffling and random state set at 1. Additionally, to minimize overfitting, during the training phase, a dropout layer with probability equal to 0.2 was added to the last hidden layer in each DNN topology.

Table 9. Topology of DNN

Layer #	Layer type	Number of neurons	Activation function
1	Input (shape 5)		
2	Dense	250	Sigmoid
3	BatchNormalization()		
4	Dense	250	Sigmoid
5	BatchNormalization()		
6	Dense	250	Sigmoid
7	Dropout (0.2)		
8	Output	2	

Assuming the goal of training is to minimize loss, the early stopping function with patience equal to 10 was added during the DNN training, in order to stop training when a monitored metric validation accuracy is stopped improving.

The overall major work was done in the PePDs' bandwidth measurement and analysis of those measurement to have proper data to simulate Li-Fi communication system, which generates relatively realistic data. The simulated dataset from Li-Fi simulation was used to train DNN to mitigate the noises mainly caused by the optoelectronic components of the system.

3. RESULTS AND DISSCUSSION

In this section the PePD's measurement analysis is provided and the influence of DNN model to the reduction of BER is also contemplated.

3.1 PePD's measurement results

The proper PD bandwidth measurement environment was designed and checked by reference PD, before measure of the bandwidth of PePDs, from Table 6. It can be seen that the measured f_{3dB} of PDA25K-EC is higher than the ones from official factory datasheets at all 4 values of TIA ampLi-Fier, which leads us conclude that there isn't any limiting device for bandwidth measurement in our setup, due to the fact that we could measure 7.75 MHz without received signal ampLi-Fication. At least, we can assume that the proved potential bandwidth of our setup is 7.75 MHz. Knowing, that we do not have any limiting factor we performed 3 different ways of PePDs bandwidth estimation and from our measurement analysis we can conclude, that 3dB frequency estimation from peak voltage measurement can be considered as a reference method, the input signal frequency steps between measurements for small PePDs were considered to be almost same and we used almost identical frequency steps for large PePDs bandwidth measurements. From the analysis of obtained data, we can clearly see that pulse rise time measurement outputs were relatively close to reference bandwidth values. However, FFT measurement is rough approximation of bandwidth, the outcomes from FFT measurements are underestimated. Each measurement is a dataset containing 2500 samples and data processing techniques were done to extract necessary data.

The estimation of PePDs bandwidth from received peak voltage measurement is regarded as a reference measurement. This is method is the most accurate one among others, since the estimation of f_{3dB} is based on the setoff 50-60 measurements, where the frequency of input signal is increasing step-by-step. The probability of the error, because received signal fluctuation, are minimized and the detection of anomaly measured peak voltage can be detect without any complexity. The important think was to compare the power response of PePDs obtained from measured peak voltage values with ideal RC filter with same f_{3dB}, which shows the quality of measurement as well as the correctness of the measurement, as an example we can see Figure 6, where power response of PePD 3 small is almost identical with RC filter behavior.

Table10. PePDs bandwidth estimation via peak voltage measurement

PePD	Offset, V	mV pp	3dB frequency, Hz	Laser wavelength, nm	surface, mm^2
3 small	6.4	220	21000	515	105
3 small	4.3	300	25500	635	105
4 small	6.4	220	30500	515	105
4 small	4.3	300	36250	635	105
2 large	6.4	220	162.5	515	1440
2 large	4.3	300	437.5	635	1440
3 large	6.4	220	450	515	1440
3 large	4.3	300	487.5	635	1440

Another approach to obtain PePDs bandwidth values was PePDs rise time measurement, this method is approximation and one measurement was performed per PePD. The reliance of this method is checked by comparison with results obtained from above mentioned method. From Table 11, it can be seen the f_{3dB} values per all 4 PePDs under both light sources.

Table11. PePDs bandwidth estimation via rise time measurement

PePD	High value , mV	Low value, mV	Peak-to-peak value, mV	$V_{10}\%, mV\ and\ T_{10}\%, \mu s$	$V_{90}\%, mV\ and\ T_{90}\%, \mu s$	3dB frequency , Hz	Offset, V	mVpp	Laser wavelength, nm	Frequency, kHz
3 small	**5.9**	**-6**	**11.9**	**-4.8 at 2751**	**4.75 at 2769**	**19021**	**6.4**	**220**	**515**	**4**
3 small	**2.955**	**-2.624**	**5.5795**	**-2.0665 at 8201.8**	**2.3971 at 8216.6**	**23648**	**4.3**	**300**	**635**	**5**
4 small	**5.9757**	**-6.060**	**12.0364**	**-4.8571 at 0.76**	**4.7721 at 12.04**	**31028**	**6.4**	**220**	**515**	**8**
4 small	**5.26**	**-4.96**	**10.22**	**-3.93 at 0.76**	**4.24 at 14.16**	**26119**	**4.3**	**300**	**635**	**7**
2 large	**67.01**	**-68**	**135**	**-54 at 8**	**53 at 1668**	**210**	**6.4**	**220**	**515**	**0.05**
2 large	**25.2**	**-25.6**	**50.8**	**-20.5 at 2**	**20.1 at 317**	**382**	**4.3**	**300**	**635**	**0.1**
3 large	**57.8**	**-50**	**107.8**	**-39 at 8**	**47 at 1124**	**313**	**6.4**	**220**	**515**	**0.05**
3 large	**29.5**	**-29.6**	**59.1**	**-23.6 at 0**	**23.6 at 880**	**397**	**4.3**	**300**	**635**	**0.1**

The last technique used to quantify the PePDs bandwidth was usage of built-in FFT function in oscillograph. This method is a rough estimation of f_{3dB} frequency of PePDs and the results of FFT method can't be considered in Li-Fi system. All values of PePDs bandwidth calculation using FFT method are underestimated and not accurate with reference ones.

Table 12. PePDs bandwidth estimation via FFT measurement

PePD	3dB frequency, Hz	Input signal frequency, Hz	Offset, V	mVpp	Duty cycle	Wavelength
3 small	15869	4000	6.4	220	1%	515
3 small	17089	5000	4.3	300	1%	635
4 small	25634	8000	6.4	220	1%	515
4 small	22071	7000	4.3	300	1%	635
2 large	36	50	6.4	220	0.1%	515
2 large	73	100	4.3	300	0.1%	635
3 large	221	100	6.4	220	0.1%	515
3 large	73	100	4.3	300	0.1%	635

Comparing the results of the measurements, it can be concluded, that the large PePDs are definitely not designed for usage within wireless communication system and their main purpose is to be implemented in future Perovskite material based solar cells and their EQE is larger than the small PePDs' due to Figure 5. According to the f_{3dB} values of both small PePDs, the small PePDs showed up higher bandwidth under red laser and PePD4 small has highest measured bandwidth f_{3dB} = 36.25kHz with surface size of PePD4 $A_{pd} = 107mm^2$, however from Figure 5 we can see the EQE of small PePDs at 635nm is slightly lower than at 515nm. One of the main advantages of Li-Fi systems is its bandwidth, that is why we can not use PePDs from our laboratory, as a solution hypothetical smaller size of PePD4 small is used to meet bandwidth requirements of the system. The bandwidth and surface size of potential PePD is calculated as follows:

$$A_{PePD} = \frac{A_{PePD4}}{\kappa} = 7.84\, mm^2, where\ \kappa = \frac{A_{PePD2}}{A_{PePD4}}; \quad (19)$$

$$f_{3dB_{PePD}} = \frac{f_{3dB_{PePD4}}}{\iota} = 2695\, kHz = 2.695\, MHz, where\ \iota = \frac{f_{3dB_{PePD4}}}{f_{3dB_{PePD2}}}; \quad (20)$$

The net-effects of the transmitter and receiver lead to a system with low-pass characteristic. The dark current value for the PePD is calculated using values from Table 7 and equals to $I_{dr} = 1.635\, \mu A$.

The minimum required distance between the transmitter and the receiver with single LED and PD is to achieve BER lower than 10^{-4} is only 0.3 meters, which is not suitable for genuine Li-Fi systems, Figure 15. The solution is to increase radiated power by adding more

LEDs in the system, that is why we designed Li-Fi with 4 LED array with N number PeLED per array. As a result we could establish acceptable communication link with the range of distance 2-3 meters.

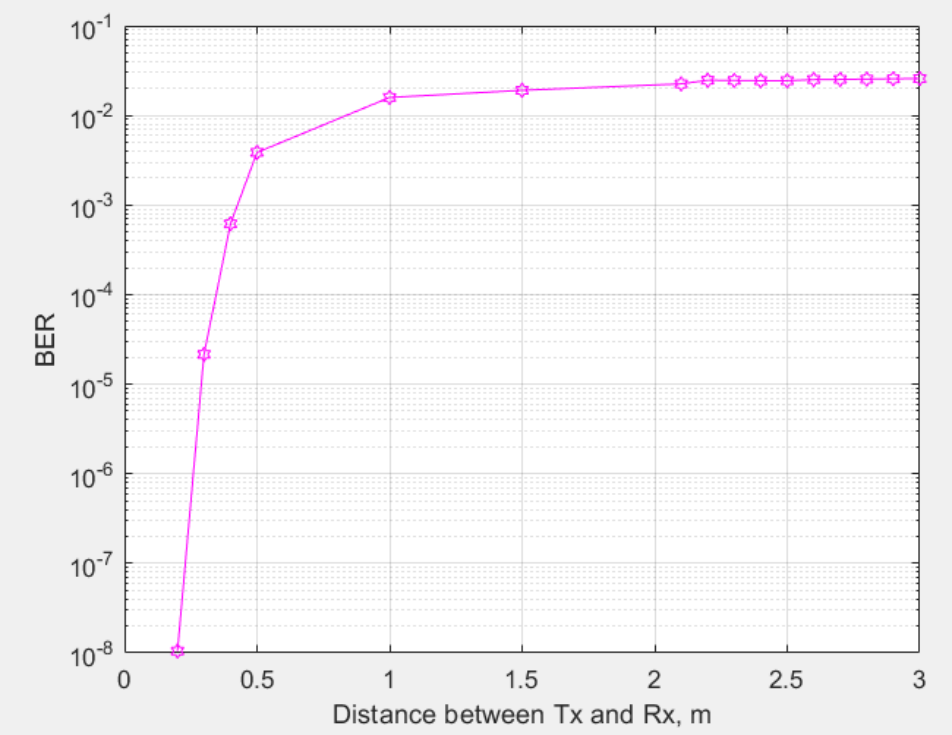

Figure 16. BER and Distance between PeLED and PePD at the angle of irradiance equal to 0.

3.2 The DNN influence evaluation

The main reason of implementation DNN is to reduce BER values at lower SNR, which will leads us use less PeLEDs per LED array. The nonlinear relationship of electrical-optical conversation in PeLED, wireless channel influence and noise at PePD disturbs received signal significantly, the mitigation of these factors is achieved by techniques as channel estimation, usage of transimpedance amplifier (TIA).

The DNN is trained by usage of K-folds cross validation method. The approach is parameterized by a single value, k, which defines the number of groups into which a given data sample should be split. As a result, k-fold cross-validation is commonly used to refer to the approach. When a specific value for k is given, it may be used in place of k in the model's reference; in this work, k=5 becomes 5-fold cross-validation. Cross-validation is frequently used in applied machine learning to determine the competency of a machine learning model on previously unknown data. That is, to test the model's general performance when used to make predictions on data that was not used during the model's training. The average validation accuracy is about 86% according the Figure 17.

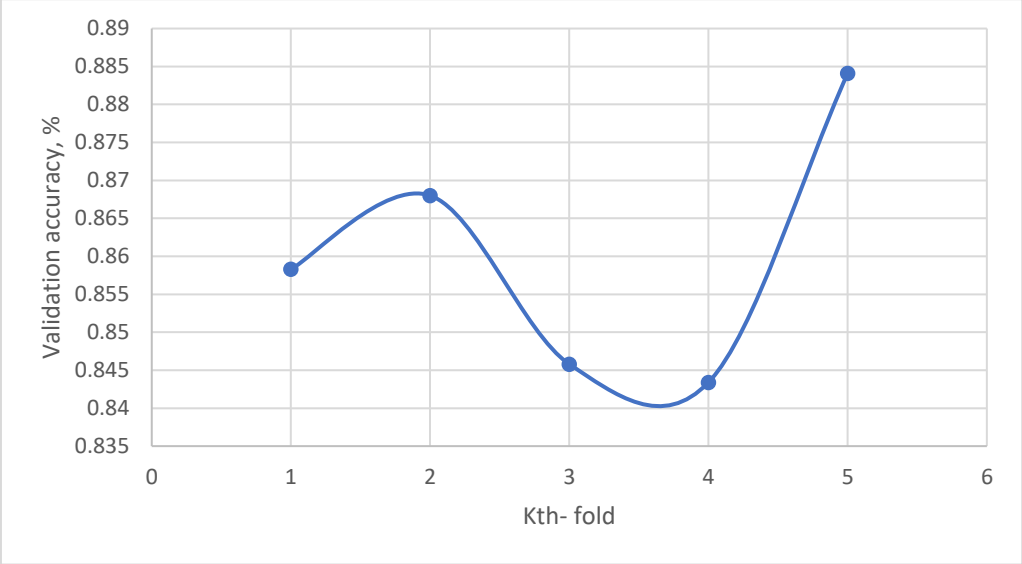

Figure 17. The 5-Fold cross validation of DNN

The influence of nonlinearities can be observed in the constellation of received 16-QAM signals. It can be noticed from figures below, that raw received signals after FFT block are highly noisy and Figure 18b, shows the high performance of DNN to mitigate the phase shifts and inter symbol interference (ISI).

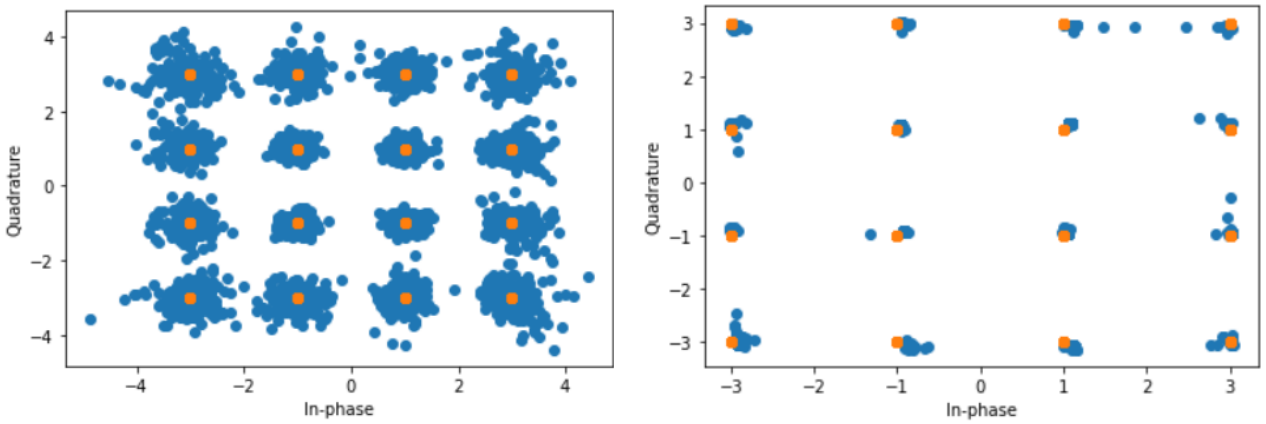

a b

Figure 18. Constellation of received 16-QAM signal before and after DNN

The evaluation the DNN performance was done by using another supervised classification algorithm Support-Vector Machines (SVM), which is widely used in the optical communications to solve problems like modulation recognition, etc. As a kernel of SVM, Radial Basis Function (RBF)' was chosen, since linear and polynomial kernels conceded to the RBF, the labels were preprocessed by K-means, to classify them into 16 clusters.

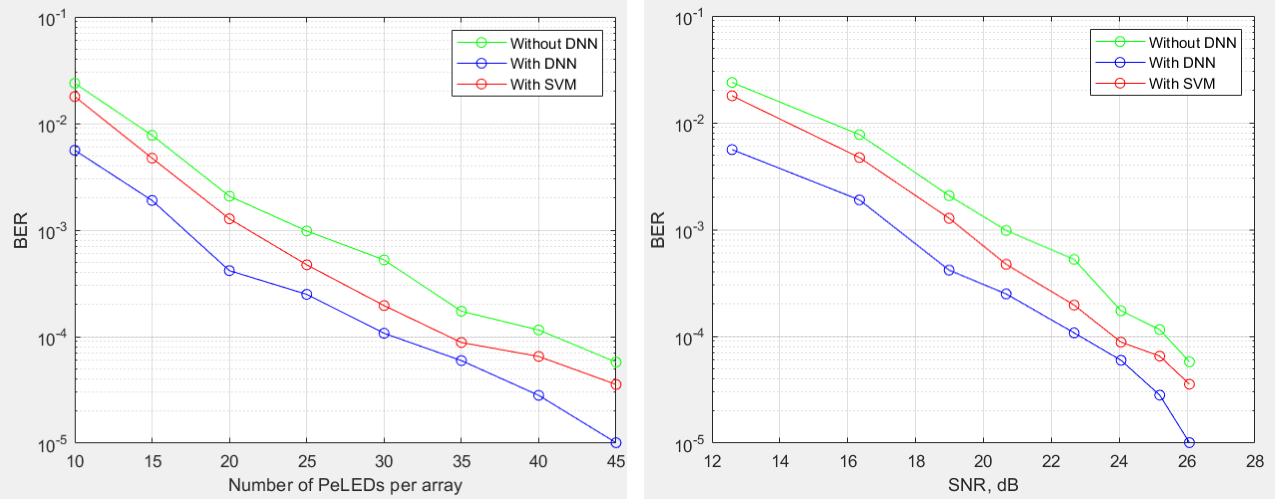

a b

Figure 19. a. BER vs Number of PeLEDs per array, b. BER vs SNR

Fig. 19 compares the BER performance of a SVM with a RBF kernel, proposed DNN with fully-connected Dense layers and Li-Fi system without any ML assistance. As can be observed, the Li-Fi system's BER reduces as the SNR grows, but there is still a notable difference between the RBF SVM's performance and DNN, SVM perform slightly lower than just Li-Fi. It can be seen that the SVM BER decreases as the SNR increases, but there is still a gap from the performance of DNN. It is can be noticed, that the results of BER without DNN shows almost same values at approximately 2dB higher SNR, Figure 19b. The new proposed DNN algorithm is improving BER by average 5 times, while SVM is showing about 2.5 times BER improvement. Figure 17 compares the received constellations of system with DNN and without DNN at SNR equal to 25dB. The DNN-based equalizer is effective in mitigating nonlinearity in a Li-Fi communication system. However, the dataset generated by the designed Li-Fi system is not sufficient enough and the Li-Fi system with Perovskite material-based devices should be performed furthermore to generate valuable dataset for future ML based solutions.

4. CONCLUSION

Over 15 years of study into physical layer approaches for LED-based VLC has resulted in the development of Li-Fi attocell networks capable of generating orders of magnitude greater data rates per unit area than current RF small cell solutions. The possible performance metrics for user data rates, number of users serviced, and increase in total traffic are all in line with 5G's and future 6G's key performance indicators. A critical component allowing this is the drastic decrease of cell sizes, which is made feasible by combining LED illumination with wireless data networking. The new wireless Li-Fi networking paradigm enables performance improvements not just in response to 5G ambitions, but also as a result of the widespread usage of LEDs, which will serve as an infrastructure for the developing IoT. Li-Fi is seen as a supplementary wireless networking approach, it may not only supply extra free and large wireless capacity, but also help to increasing the spectrum efficiency of current radio frequency networks. Additionally, this work demonstrated for the potential of Perovskite based LEDs and PDs within Li-Fi communication system and deeper research in implementation of these devices in Li-Fi along with introduction of Deep Learning models will lead us to design commercial solution for last mile wireless networks in future 6G networks.

To summarize, the Li-Fi communication system was simulated with usage of Perovskite based LED and PD characteristics and regarding PePD, a bandwidth measurement of PePD was completed via 3 different methods and due to the analysis of the results, peak voltage measurement was chosen as a reference technique. The highest cutting-off frequency $f_{3dB} = 36.25kHz$ of small PePD4 was measured at 625nm wavelength, taking into the simulation of Li-Fi with large enough bandwidth for data transfer, the potential smaller size PePD surface size, and bandwidth was calculated by usage of the data from the measurements. Resulting Li-Fi system bandwidth is considered to be 1.9MHz, which is the taken from PeLED characteristics, Table [2]. All the measurements and measurement analysis scripts were uploaded in the cloud.

The Li-Fi physical layer was represented by the over-the-air interface simulation including the channel, modulation and coding schemes, and packet reception metrics. For the channel, the optical channel consisting of the LOS and non-LOS (NLOS) components were considered. For the modulation, we considered the modulation scheme Flip-OFDM, which is unipolar modulation technique and 16-QAM mapping was used.

To reduce the PeLED nonlinearity in an OFDM-based Li-Fi system, a deep learning model has been suggested. The simulation findings demonstrate that the proposed DNN successfully mitigates nonlinear distortions, including PeLED, PePD, and also rectifies the ISI produced by the multipath of the IM/DD channel. Due to the incorporation of expert-domain knowledge from [29,56,57], the DNN outperforms the basic-Li-Fi approach in terms of BER. To have a better evaluation of DNN model, SVM ML algorithms was used for fine categorization of noisy 16-QAM modulated signal, the performance of SVM model is slightly superior against solely Li-Fi without any ML assistance, but DNN model remarkably outperforms both SVM based Li-Fi model and Li-Fi without any ML. Additionally, the DNN may continue to function successfully with lower SNR, owing to the tremendous learning potential of DL, which overcomes the decencies inherent in real communications. This work provides a preliminary examination of the DL applications on physical layer communications. Additional rigorous research and extensive experiments, such as deeper theoretical study of

the DNN based Li-Fi system, are required to fine-tune the DNN model for improved BER performance and for overcoming network training's unpredictability and instability.

ABBREVIATIONS – ACRONYMS

ML	Machine Learning
AI	Artificial Intelligence
Li-Fi	Light Fidelity
VLC	Visual Light Communication
DNN	Deep Neural Networks
PePD	Perovskite Photodiode
SVM	Support Vector Machines
RF	Radio Frequency
LED	Laser Emitting Diode
EQE	External Quantum Efficiency
OFDM	Orthogonal Frequency Division Multiplexing
MLP	Multiple Layer Perception
BER	Bit Error Rate
PeLED	Perovskite Laser Emitting Diode
SNR	Signal to Noise Ratio
FFT	Fast Fourier Transform
DD	Direct Detection
IM	Intensity Modulation
QAM	Quadrature Amplitude Modulation
CCI	Co-Channel Interference
MAC	Medium Access Control
UE	User Equipment
AP	Access Point
MIMO	Multiple Input Multiple Output
LCA	Light Communication Alliance
SCM	Single Carrier Modulation
OOK	On-Off Keying
PAM	Pulse Amplitude Modulation
MCM	Multiple Carrier Modulation
ACO	Asymmetric Clipped Optical

DFT	Discrete Fourier Transform
FOV	Field of View
LOS	Line of Sight
NLOS	Non-LOS
RBF	Radial Basis Function

ANNEX I

Source code for DNN model in python

```
#Importing libraries
import matplotlib.pyplot as plt
import numpy as np
from numpy import genfromtxt
from numpy import savetxt
import pandas as pd

import tensorflow
import tensorflow.keras
import math
from sklearn import metrics
from sklearn.svm import SVC
from sklearn import svm
import sklearn

import tensorflow as tf
from tensorflow.keras import layers
from sklearn.model_selection import train_test_split
from sklearn.model_selection import StratifiedKFold, KFold
from sklearn.preprocessing import MinMaxScaler
from tensorflow.keras.models import Sequential, load_model
from tensorflow.keras.layers import Dense ,BatchNormalization, Dropout
from tensorflow.keras.layers import Dropout
from tensorflow.keras.initializers import RandomNormal, Constant
from keras.utils.vis_utils import plot_model
from sklearn import metrics

# Importing dataset
X_training = []
X = []
# import label data as an array of strings using the dtype
mod_signal = genfromtxt('C:/Users/bxoji/ML assisted Li-Fi/Mod_10sym.csv',
delimiter=',',dtype='str')
# perform elementwise conversion to complex numpers
mapping_1 = np.vectorize(lambda t:complex(t.replace('i','j')))
Y_label = mapping_1(mod_signal)
# import noisy data as an array of strings using the dtype
rec_mod_signal = genfromtxt('C:/Users/bxoji/ML assisted Li-Fi/Rec_Mod_10sym.csv',
delimiter=',',dtype='str')
# perform elementwise conversion to complex numpers
mapping_2 = np.vectorize(lambda t:complex(t.replace('i','j')))
X = mapping_2(rec_mod_signal)

# Data preparation, separating Real and Imaginary parts
Y_label_img1 = Y_label.imag
Y_label_real1 = Y_label.real

X_img1 = X.imag
X_real1 = X.real

X_real = X_real1.reshape(51100,1)
X_img = X_img1.reshape(51100,1)
Y_label_img = Y_label_img1.reshape(51100,1)
Y_label_real = Y_label_real1.reshape(51100,1)
```

```
#Feature Extraction
X_real_sq = np.square(X_real)
X_img_sq = np.square(X_img)
X_abs = np.sqrt(X_real_sq + X_img_sq)

x = np.concatenate((X_img, X_real), axis=1)
x = np.concatenate((x, X_real_sq), axis=1)
x = np.concatenate((x, X_img_sq), axis=1)
x = np.concatenate((x, X_abs), axis=1)
y = np.concatenate((Y_label_img, Y_label_real), axis =1)

# DNN Model creation
tf.compat.v1.reset_default_graph()
inputs = tf.keras.Input(shape=(5))

xx = tf.keras.layers.Dense(250, activation='sigmoid')(inputs)
xx = BatchNormalization(xx)
xx = tf.keras.layers.Dense(250, activation='sigmoid')(xx)
xx = BatchNormalization()(xx)
xx = tf.keras.layers.Dense(250, activation='sigmoid')(xx)
xx = tf.keras.layers.Dropout(0.2)(xx)
outputs = tf.keras.layers.Dense(2, name='predictions', use_bias=False)(xx)

model = tf.keras.Model(inputs=inputs, outputs=outputs)
model.compile(optimizer=tf.keras.optimizers.Adam(learning_rate=0.001),
          loss= tf.keras.losses.mean_squared_error, #tf.keras.losses.categorical_crossentropy,
#'binary_crossentropy',
          metrics=['accuracy'])
scores = []
es =tf.keras.callbacks.EarlyStopping(monitor='accuracy', mode='max', verbose=0, patience=10)

# Model training
for k in range(5):
  X_d_train, X_d_test, y_train, y_test = train_test_split(x, y, test_size=0.2, random_state=k+10)

  model.fit(X_d_train, y_train, batch_size = 250, epochs = 100, verbose = 1, callbacks=[es])

  predictions = model.predict(X_d_test)

  accuracy = model.evaluate(X_d_test, y_test)
  scores.append(accuracy[1] * 100)

plt.plot(scores)
plt.title('model accuracy')
plt.yticks(np.arange(0,100,step=5))
plt.xticks(np.arange(0,len(val_scores),step=1))
plt.ylabel('accuracy %')
plt.xlabel('Kth fold')
plt.legend(['test_acc','train_acc'], loc = 'lower left')
plt.grid()
plt.show()
```

Source code for SVM model in python

```
# Data preparation

from sklearn.cluster import KMeans
data = np.arange(51100, dtype='float64')
X_real = X_real.reshape(51100,1)
X_img = X_img.reshape(51100,1)
data = np.concatenate((X_real, X_img), axis=1)
data = data.reshape(51100,2)*100

# Creation labels using K-means
Y_labels = np.arange(51100, dtype='float64')
Y_label_real = Y_label_real.reshape(51100,1)
Y_label_img = Y_label_img.reshape(51100,1)
Y_labels = np.concatenate((Y_label_real, Y_label_img), axis=1)
Y_labels = Y_labels.reshape(51100,2)

kmeans = KMeans(n_clusters=16,init='random')
kmeans.fit(Y_labels)
Y_labels = kmeans.predict(Y_labels)
Y_labels = Y_labels.astype('float64')

centroids = kmeans.cluster_centers_
labels= kmeans.labels_

# Spliting data into train & test sections
X_train, X_test, y_train, y_test = sklearn.model_selection.train_test_split(data, Y_labels,
test_size=0.33, random_state=42)
# SVM regularization parameter
C = 1
# Model training
svc = SVC(kernel='rbf', C=C).fit(X_train, y_train)
predicted = svc.predict(X_test)
accuracy = metrics.accuracy_score(y_test, predicted)
X_ml = svc.predict(data)
print(accuracy)

# Predicted dataset preparation
X_ml_img = np.zeros(5110, dtype='float64')
X_ml_real = np.zeros(5110, dtype='float64')
X_ml = X_ml.astype('complex')
for i in range(X_ml.size):
    if X_ml[i]==0:
        X_ml_img[i] = centroids[0,1]
        X_ml_real[i] = centroids[0,0]
        X_ml[i] = complex(X_ml_real[i], X_ml_img[i])
    if X_ml[i]==1:
        X_ml_img[i] = centroids[1,1]
        X_ml_real[i] = centroids[1,0]
        X_ml[i] = complex(X_ml_real[i], X_ml_img[i])
    if X_ml[i]==2:
        X_ml_img[i] = centroids[2,1]
        X_ml_real[i] = centroids[2,0]
        X_ml[i] = complex(X_ml_real[i], X_ml_img[i])
    if X_ml[i]==3:
        X_ml_img[i] = centroids[3,1]
        X_ml_real[i] = centroids[3,0]
```

```
        X_ml[i] = complex(X_ml_real[i], X_ml_img[i])
    if X_ml[i]==4:
        X_ml_img[i] = centroids[4,1]
        X_ml_real[i] = centroids[4,0]
        X_ml[i] = complex(X_ml_real[i], X_ml_img[i])
    if X_ml[i]==5:
        X_ml_img[i] = centroids[5,1]
        X_ml_real[i] = centroids[5,0]
        X_ml[i] = complex(X_ml_real[i], X_ml_img[i])
    if X_ml[i]==6:
        X_ml_img[i] = centroids[6,1]
        X_ml_real[i] = centroids[6,0]
        X_ml[i] = complex(X_ml_real[i], X_ml_img[i])
    if X_ml[i]==7:
        X_ml_img[i] = centroids[7,1]
        X_ml_real[i] = centroids[7,0]
        X_ml[i] = complex(X_ml_real[i], X_ml_img[i])
    if X_ml[i]==8:
        X_ml_img[i] = centroids[8,1]
        X_ml_real[i] = centroids[8,0]
        X_ml[i] = complex(X_ml_real[i], X_ml_img[i])
    if X_ml[i]==9:
        X_ml_img[i] = centroids[9,1]
        X_ml_real[i] = centroids[9,0]
        X_ml[i] = complex(X_ml_real[i], X_ml_img[i])
    if X_ml[i]==10:
        X_ml_img[i] = centroids[10,1]
        X_ml_real[i] = centroids[10,0]
        X_ml[i] = complex(X_ml_real[i], X_ml_img[i])
    if X_ml[i]==11:
        X_ml_img[i] = centroids[11,1]
        X_ml_real[i] = centroids[11,0]
        X_ml[i] = complex(X_ml_real[i], X_ml_img[i])
    if X_ml[i]==12:
        X_ml_img[i] = centroids[12,1]
        X_ml_real[i] = centroids[12,0]
        X_ml[i] = complex(X_ml_real[i], X_ml_img[i])
    if X_ml[i]==13:
        X_ml_img[i] = centroids[13,1]
        X_ml_real[i] = centroids[13,0]
        X_ml[i] = complex(X_ml_real[i], X_ml_img[i])
    if X_ml[i]==14:
        X_ml_img[i] = centroids[14,1]
        X_ml_real[i] = centroids[14,0]
        X_ml[i] = complex(X_ml_real[i], X_ml_img[i])
    if X_ml[i]==15:
        X_ml_img[i] = centroids[15,1]
        X_ml_real[i] = centroids[15,0]
        X_ml[i] = complex(X_ml_real[i], X_ml_img[i])

#Saving predicted data
print("Accuracy:",metrics.accuracy_score(Y_labels, Z))
X_ml_img = np.reshape(X_ml_img, (511,100))
X_ml_real = np.reshape(X_ml_real, (511,100))
savetxt('C:/Users/bxoji/OneDrive/Documents/Internship/Transreceiver/Rec_Mod_ML_img.csv',
X_ml_img, delimiter=',',fmt='%s')
savetxt('C:/Users/bxoji/OneDrive/Documents/Internship/Transreceiver/Rec_Mod_ML_real.csv',
X_ml_real, delimiter=',',fmt='%s')
print(X_ml)
```

Source code for data extraction from measurements for PePD4 small at 635nm in python

```
#Importing libraries
import pandas as pd
import matplotlib.pyplot as plt
import os
import numpy as np
import numpy.fft as fft

#Reading data from measurements
PePD4_small_2 = 'D:/Documents/Smartnet/Subjects/Semester 4th/Analysis of Measurements/Final measurements/PePD_4_small_at_red'
Folder_Amount = []
Amplitude = []
Amp = pd.DataFrame()


dirListing = os.listdir(PePD4_small_2)

for j in range(len(dirListing) - 4):
    if j>9:
        full_path = PePD4_small_2 + '/ALL00' + str(j) + '/F00' + str(j) + 'CH1.csv'
    else:
        full_path = PePD4_small_2 + '/ALL000' + str(j) + '/F000' + str(j) + 'CH1.csv'
    df = pd.read_csv(full_path)
    if len(df.columns) > 5:
        df.columns = ("Parameters","Scale", "Empty", "Time", "Amplitude","Empty")
    else:
        df.columns = ("Parameters","Scale", "Empty", "Time", "Amplitude")
    Amplitude.append(max(df['Amplitude']))
Amplitude = pd.DataFrame(Amplitude,columns=['Amplitude'])
print(Amplitude)
Amplitude.to_csv(path_or_buf = 'D:/Documents/Smartnet/Subjects/Semester 4th/Analysis of Measurements/Final measurements/PePD_4_small_at_red/amp_PePD4_small_red.csv', index = False)
```

ANNEX II

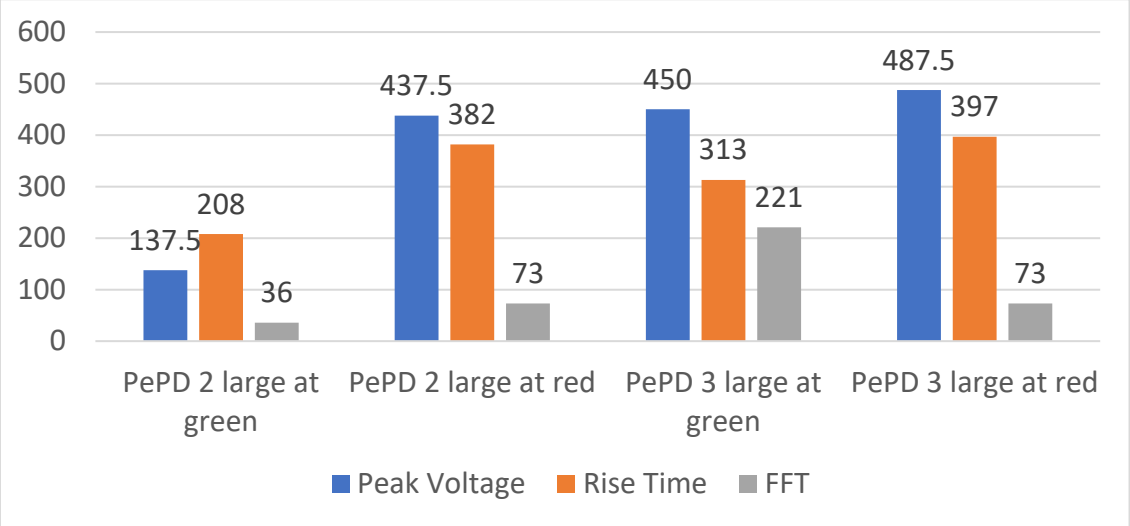

Figure 19. Values of large PePDs bandwidth thought different methods

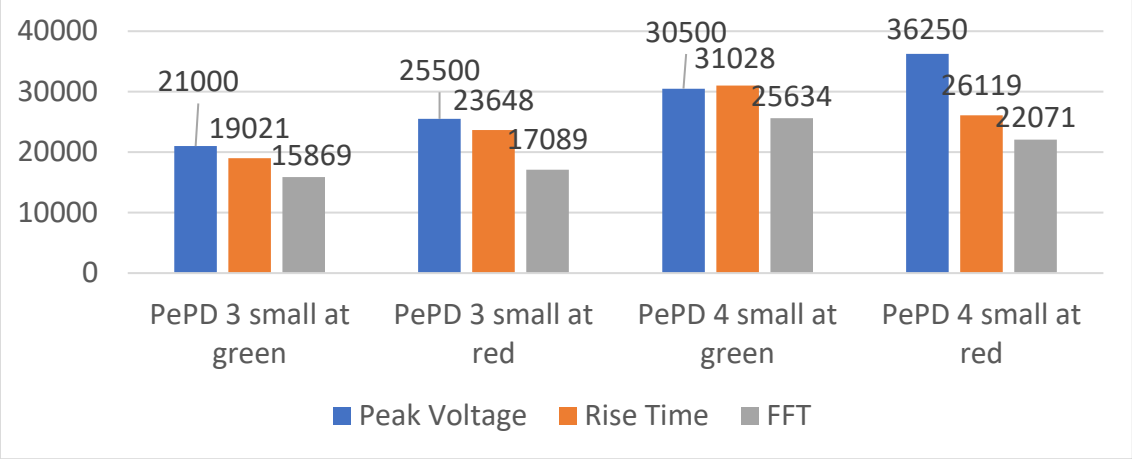

Figure 20. Values of small PePDs bandwidth thought different methods

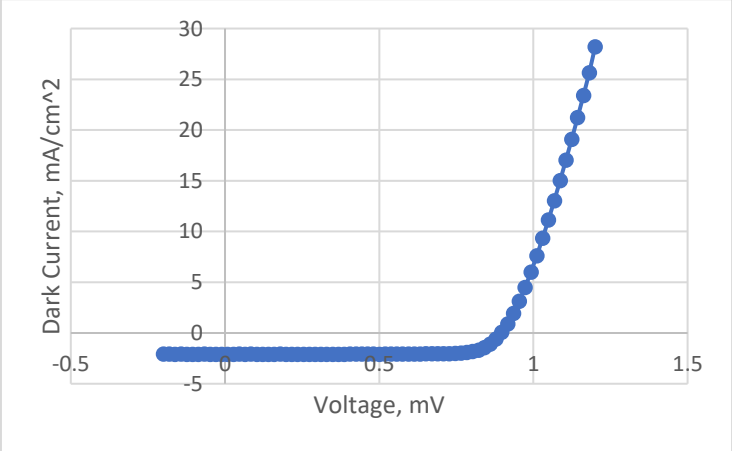

Figure 21. PePD4 small Dark Current vs Voltage

REFERENCES

[1] Kaushal, H. and Kaddoum, G., 2017. *Optical Communication in Space: Challenges and Mitigation Techniques*. *IEEE Communications Surveys & Tutorials*, 19(1), pp.57-96.

[2] Haas, H., 2018. Li-Fi is a paradigm-shifting 5G technology. *Reviews in Physics*, 3, pp.26-31.

[3] Rahman, M., Bakibillah, A., Parthiban, R. and Bakaul, M., 2020. *Review of advanced techniques for multi-gigabit visible light communication*. *IET Optoelectronics*, 14(6), pp.359-373.

[4] D. Hochfelder, "Alexander graham bell," Encylopedia Britannica, 2015.

[5] D. L. Hutt, K. J. Snell, and P. A. Belanger, "*Alexander graham bell's photophone*," Tech. Report: Optic & Photonics News, 1993.

[6] Rajagopal, S., Roberts, R. and Lim, S., 2012. *IEEE 802.15.7 visible light communication: modulation schemes and dimming support. IEEE Communications Magazine*, 50(3), pp.72-82.

[7] E. Sarbazi, M. Uysal, M. Abdallah, and K. Qaraqe, "*Ray tracing based channel modeling for visible light communications*," in *Proc. 22nd Signal Process. Commun. Appl. Conf.*, Apr. 2014, pp. 702–705.

[8] A. Farid and S. Hranilovic, "*Capacity bounds for wireless optical intensity channels with Gaussian noise*," *IEEE Trans. Inf. Theory*, vol. 56, no. 12, pp. 6066–6077, Dec. 2010.

[9] IEEE Std. 802.15.7-2011, *IEEE Standard for Local and Metropolitan Area Networks, Part 15.7: Short-Range Wireless Optical Communication Using Visible Light*, IEEE Std., 2011.

[10] R. Mesleh, H. Elgala, and H. Haas, "*Optical spatial modulation*," IEEE/OSA J. Opt. Commun. Netw., vol. 3, no. 3, pp. 234–244, Mar. 2011.

[11] F.-M. Wu, C.-T. Lin, C.-C. Wei, C.-W. Chen, H.-T. Huang, and C.-H. Ho, "*1.1-Gb/s white-LED-based visible light communication Employing carrier-less amplitude and phase modulation*," IEEE Photon. Technol. Lett., vol. 24, no. 19, pp. 1730–1732, Oct. 2012.

[12] T. Komine, S. Haruyama, and M. Nakagawa, "*Performance evaluation of narrowband OFDM on integrated system of power line communication and visible light wireless communication*," in Proc. Int. Symp. Wireless Pervasive Comput., Jan. 2006, doi: 10.1109/ISWPC.2006.1613633.

[13] J. Armstrong and A. Lowery, "*Power efficient optical OFDM*," Electronics Letters, vol. 42, no. 6, pp. 370–372, 2006.

[14] Miao, J. and Zhang, F., 2019. *Recent progress on highly sensitive perovskite photodetectors*. Journal of Materials Chemistry C, 7(7), pp.1741-1791.

[15] Ahmadi, M., Wu, T. and Hu, B., 2017. *A Review on Organic–Inorganic Halide Perovskite Photodetectors: Device Engineering and Fundamental Physics. Advanced Materials*, 29(41), p.1605242.

[16] Li, C., Wang, H., Wang, F., Li, T., Xu, M., Wang, H., Wang, Z., Zhan, X., Hu, W. and Shen, L., 2020. *Ultrafast and broadband photodetectors based on a perovskite/organic bulk heterojunction for large-dynamic-range imagin*g. Light: Science & Applications, 9(1).

[17] Y. Wang, X. Li, J. Song, L. Xiao, H. Zeng and H. Sun, *All-inorganic colloidal perovskite quantum dots: a new class of lasing materials with favorable characteristics*, Adv. Mater., 2015, 27(44), 7101–7108.

[18] S. H. Turren-Cruz, A. Hagfeldt and M. Saliba, *Methylammonium-free, high-performance, and stable perovskite solar cells on a planar architecture*, Science, 2018, 362(6413), 449–453. X. Zhao and N. G. Park, Stability issues on perovskite solar cells, Photonics, 2015, 2, 1139–1151.

[19] K. Domanski, J. P. Correa-Baena, N. Mine, M. K. Nazeeruddin, A. Abate, M. Saliba, W. Tress, A. Hagfeldt and M. Grätzel, *Not all that glitters is gold: metal-migration-induced degradation in perovskite solar cells*, ACS Nano, 2016, 10(6), 6306–6314.

[20] C. L. Tsai, Y. C. Lu and S. H. Chang, *Enhancement of photocurrent extraction and electron injection in dualfunctional CH3NH3PbBr3 perovskite-based optoelectronic devices via interfacial engineering*, Nanotechnology, 2018, 29(27), 275704.

[21] G. Namkoong, A. A. Mamun and T. T. Ava, *Impact of PCBM/C60 electron transfer layer on charge transports on ordered and disordered perovskite phases and hysteresis free perovskite solar cells*, Org. Electron., 2018, 56, 163–169.

[22] C. Li, Z. Zang, W. Chen, Z. Hu, X. Tang, W. Hu, K. Sun, X. Liu and W. Chen, *Highly pure green light emission of perovskite CsPbBr3 quantum dots and their application for green light-emitting diodes*, Opt. Express, 2016, 24(13), 15071–15078.

[23] J. Troughton, K. Hooper and T. M. Watson, *Humidity resistant fabrication of CH3NH3PbI3 perovskite solar cells and modules*, Nano Energy, 2017, 39, 60–68.

[24] W. Ming, D. Yang, T. Li, L. Zhang and M. H. Du, *Formation and diffusion of metal impurities in perovskite solar cell material CH3NH3PbI3: implications on solar cell degradation and choice of electrode*, Adv. Sci., 2018, 5(2), 1700662.
[25] H. Huang, F. Zhao, L. Liu, F. Zhang, X. G. Wu, L. Shi, B. Zo, Q. Pei and H. Zhong, *Emulsion synthesis of size-tunable CH3NH3PbBr3 quantum dots: an alternative route toward efficient light-emitting diodes*, ACS Appl. Mater. Interfaces, 2015, 7(51), 28128–28133.
[26] Tsai, C., Lu, Y., Chiang, S., Yu, C., Cheng, H., Hsu, C., Chiu, K. and Chang, S., 2020. *Bright and fast-response perovskite light-emitting diodes with an ICBA:modified-C60 nanocomposite electrical confinement layer*. Nanoscale, 12(6), pp.4061-4068.
[27] K. Y. Chiu, S. H. Chang, W. C. Huang, H. M. Cheng, H. Shaw, S. C. Yeh, C. T. Chen, Y. O. Su, S. H. Chen and C. G. Wu, *Functional graded fullerene derivatives for improving the fill factor and device stability of invertedtype perovskite solar cells*, Nanotechnology, 2018, 29(30), 305701.
[28] N. Chi, J. Jia, F. Hu, Y. Zhao and P. Zou, "*Challenges and prospects of machine learning in visible light communication*," in *Journal of Communications and Information Networks*, vol. 5, no. 3, pp. 302-309, Sept. 2020, doi: 10.23919/JCIN.2020.9200893.
[29] BISHOP C M. *Pattern recognition and machine learning*[M]. Berlin: Springer, 2006.
[30] WANG Y, TAO L, HUANG X, et al. *8-Gb/s RGBY LED-based WDM VLC system employing high-order CAP modulation and hybrid post equalizer*[J]. IEEE Photonics Journal, 2015, 7(6): 1-7.
[31] KHAN F N, LU C, LAU A P T. *Machine learning methods for optical communication systems[C]//Signal Processing in Photonic Communications*. Washington D. C.: Optical Society of America, 2017: SpW2F-3.
[32] R. Bian, I. Tavakkolnia, and H. Haas, "*15.73Gb/s visible light communication with off-the-shelf LEDs*," J. Lightw. Technol., vol.37, no.10, pp. 2418-2424, May 2019.
[33] Cisco, "Cisco Annual Internet Report (2018-2023) White Paper", 2020.
[34] "LOI n 2015-136 du 9 f´evrier 2015 ("Loi Abeille")", JORF, no. 0034, p.2346, Feb 2015.
[35] Bao, C., Xu, W., Yang, J., Bai, S., Teng, P., Yang, Y., Wang, J., Zhao, N., Zhang, W., Huang, W. and Gao, F., 2020. *Bidirectional optical signal transmission between two identical devices using perovskite diodes*. *Nature Electronics*, 3(3), pp.156-164.
[36] Clifford, J. P. et al. *Fast, sensitive and spectrally tuneable colloidal-quantumdot photodetectors*. *Nat. Nanotechnol.* **4**, 40–44 (2009).
[37] Tan, Z. K. et al. *Bright light-emitting diodes based on organometal halide perovskite*. *Nat. Nanotechnol.* **9**, 687–692 (2014).
[38] Sutherland, B. R. & Sargent, E. H. Perovskite photonic sources. *Nat. Photonics* **10**, 295–302 (2016).
[39] Dou, L. et al. *Solution-processed hybrid perovskite photodetectors with high detectivity*. *Nat. Commun.* **5**, 5404 (2014).
[40] Feng, J. et al. *Single-crystalline layered metal–halide perovskite nanowires for ultrasensitive photodetectors*. *Nat. Electron.* **1**, 404–410 (2018).
[41] Shen, L. et al. *A self-powered, sub-nanosecond-response solution-processed hybrid perovskite photodetector for time-resolved photoluminescence-lifetime detection*. *Adv. Mater.* **28**, 10794–10800 (2016).
[42] Bao, C. et al. *Low-noise and large-linear-dynamic-range photodetectors based on hybrid-perovskite thin-single-crystals*. *Adv. Mater.* **29**, 1703209 (2017).
[43] Chiba, T. et al. *Anion-exchange red perovskite quantum dots with ammonium iodine salts for highly efficient light-emitting devices*. *Nat. Photonics* **12**, 681–687 (2018).
[44] Zhao, B. et al. *High-efficiency perovskite–polymer bulk heterostructure light-emitting diodes*. *Nat. Photonics* **12**, 783–789 (2018).
[45] Cao, Y. et al. *Perovskite light-emitting diodes based on spontaneously formed submicrometre-scale structures*. *Nature* **562**, 249–253 (2018).
[46] Lin, K. et al. *Perovskite light-emitting diodes with external quantum efficiency exceeding 20 per cent*. *Nature* **562**, 245–248 (2018).
[47] Xu, W. et al. *Rational molecular passivation for high-performance perovskite light-emitting diodes*. *Nat. Photonics* **13**, 418–424 (2019).
[48] Liao, C., Chang, Y., Ho, C. and Wu, M., 2013. *High-Speed GaN-Based Blue Light-Emitting Diodes With Gallium-Doped ZnO Current Spreading Layer*. *IEEE Electron Device Letters*, 34(5), pp.611-613.
[49] Liao, C. L., Ho, C. L., Chang, Y. F., Wu, C. H. & Wu, M. C. *High-speed light-emitting diodes emitting at 500 nm with 463-Mhz modulation bandwidth. IEEE Electron Device Lett.* **35**, 563–565 (2014).

[50] Kim, J. S., Kajii, H. & Ohmori, Y. *Characteristics of optical response in red organic light-emitting diodes using two dopant system for application to the optical link devices*. *Thin Solid Films* **499**, 343–348 (2006).
[51] 2017. *PDA25K(-EC) GaP Switchable Gain Detector*. 1st ed. ThorLabs.
[52] 2021. *PLT5 510 Metal Can® TO56 Green Laser Diode in TO56 Package*. OSRAM Opto Semiconductors GmbH.
[53] 2019. *635nm Red Single Mode Laser Diode RLD63NPC5*. ROHM Co., Ltd.
[54] Qiu, Y., Chen, H. and Meng, W., 2016. *Channel modeling for visible light communications-a survey*. *Wireless Communications and Mobile Computing*, 16(14), pp.2016-2034.
[55] N. Fernando, Y. Hong and E. Viterbo, "*Flip-OFDM for optical wireless communications*," *2011 IEEE Information Theory Workshop*, 2011, pp. 5-9, doi: 10.1109/ITW.2011.6089566.
[56] S. Dörner, S. Cammerer, J. Hoydis, and S. ten Brink, ``*Deep learning based communication over the air,*'' *IEEE J. Sel. Topics Signal Process.*, vol. 12, no. 1, pp. 132_143, Feb. 2018.
[57] T. Wang, C.-K. Wen, H. Wang, F. Gao, T. Jiang, and S. Jin, ``*Deep learning for wireless physical layer: Opportunities and challenges*,'' *China Commun.*, vol. 14, no. 11, pp. 92_111, 2017.